Newsletters on Stratigraphy, Vol. 56/4 (2023), 457–484
Published online April 12, 2023; published in print September 2023

Open Access Article

Astrochronology of the Miocene Climatic Optimum record from Ocean Drilling Program Site 959 in the eastern equatorial Atlantic

Evi Wubben[1]*, Tjerk Veenstra[1], Jakub Witkowski[2], Isabella Raffi[3], Frederik Hilgen[1], Remco Bos[1], Joost van Dijk[1], Ymke Lathouwers[1], Bianca Spiering[1], Laurens Vennema[1], Zongyi Wang[1], Francesca Sangiorgi[1] and Appy Sluijs[1]

With 10 figures and 1 table

Abstract. The Miocene Climatic Optimum (MCO; ~16.9–14.7 Ma) was a relatively warm interval which interrupted the Cenozoic cooling trend and bears analogies with projected near-future climate change. Evidence for MCO warming and climatic variability is dominantly based on studies from mid- to high-latitude regions and deep ocean benthic foraminiferal oxygen isotope reconstructions, whereas studies from tropical latitudes are needed to resolve latitudinal temperature gradients and ocean nutrient cycling. Sedimentary cores retrieved at Ocean Drilling Program (ODP) Site 959 (Leg 159) in the eastern equatorial Atlantic Ocean offer a near-continuous, low-latitude record spanning the Early to Middle Miocene, but age constraints were limited. To achieve an orbitally resolved age model, we generated new calcareous nannofossil and diatom biostratigraphy as well as high-resolution bulk carbonate stable carbon ($\delta^{13}C$) and oxygen isotope ($\delta^{18}O$) ratios, magnetic susceptibility (MS), weight percent $CaCO_3$ and mean greyscale records. We record several diagnostic biostratigraphic markers and identify the well-dated onset of the MCO, Monterey Excursion (ME), Carbon Maxima (CM) events and *peak warming* in the bulk carbonate isotope records. An orbital age model is realized by tuning the bulk carbonate $\delta^{13}C$ record to eccentricity extracted from the Laskar et al. (2004) astronomical solution that is consistent with the bio- and chemostratigraphic constraints. We conclude that the studied sediment record spans the Early to Middle Miocene interval between ~18.2 and 15 Ma and includes a hiatus directly prior to the onset of MCO of maximally ~700 kyr. All records reveal dominant eccentricity-paced variability, while prominent precession and obliquity paced variability is observed between ~16.9–16.1 Ma; this interval corresponds to a node in the long ~2.4 Myr eccentricity cycle. Moreover, a major shift from bio-siliceous-dominated to carbonate-rich sediments is found across the onset of the MCO (~16.9 Ma). Both lithologies represent intervals of relatively high productivity, likely associated with upwelling. Ultimately, our high-resolution record from Site 959 can provide an important opportunity for reconstructing a tropical paleoclimate record at precession-to-eccentricity resolution during the MCO.

Key words. Miocene Climatic Optimum, bulk carbonate isotope stratigraphy, biostratigraphy, Ocean Drilling Program Site 959, astronomical tuning, Monterey Excursion, eccentricity

Authors' addresses:
[1] Department of Earth Sciences, Faculty of Geosciences, Utrecht University, Princetonlaan 8, 3584 CB Utrecht, The Netherlands
[2] Institute of Marine and Environmental Sciences, University of Szczecin, ul. Mickiewicza 18, 70-383 Szczecin, Poland
[3] Dipartimento di Ingegneria e Geologia, Università degli Studi 'G. d'Annunzio' Chieti–Pescara, via dei Vestini 31, 66013 Chieti-Pescara, Italy
* Corresponding author: e.wubben@uu.nl

© 2023 The Authors

DOI: 10.1127/nos/2023/0749 Borntraeger Science Publishers, Stuttgart, www.borntraeger-cramer.com

1. Introduction

1.1. The Miocene Climatic Optimum

The Miocene epoch is characterized by phases of significant warming, which followed long-term Eocene cooling and relative stability during the Oligocene, as recorded in benthic foraminiferal oxygen isotope ratios ($\delta^{18}O$) and surface temperature records (Vincent and Berger 1985, de Vleeschouwer et al. 2017, Cramwinckel et al. 2018, Westerhold et al. 2020, Gaskell et al. 2022). The Early Miocene stands out because of the Miocene Climatic Optimum (MCO; ~16.9–14.7 Ma), an episode of significant warming, which terminated in stepwise cooling and increased global ice volume across the Mid Miocene Climatic Transition (MMCT; ~14.7–13.8 Ma) (Woodruff and Savin 1991, Flower and Kennett 1993, Flower and Kennett 1994, Shevenell et al. 2008). The MCO is recognized by an abrupt ~1‰ decrease in global deep ocean benthic foraminiferal $\delta^{18}O$ (Woodruff and Savin 1991, Billups et al. 2002, Holbourn et al. 2007, Holbourn et al. 2015, Kochhann et al. 2016). Widespread warming is inferred from geochemical records (Mg/Ca: Sosdian et al. 2018, Hollis et al. 2019, Miller et al. 2020, Modestou et al. 2020; TEX_{86}: Levy et al. 2016, Super et al. 2018, Super et al. 2020, Sangiorgi et al. 2018, Sangiorgi et al. 2021; $U^{k'}_{37}$: Guitián et al. 2019, Sangiorgi et al. 2021) and biogeographic patterns (i. e., global vegetation patterns: Warny et al. 2009, Pound et al. 2012, Hui et al. 2018, Sangiorgi et al. 2018). Together with model reconstructions, these proxy paleotemperatures suggest that global climate during the MCO was ~7–8 °C warmer than present day (Lear et al. 2000, You et al. 2009, Sangiorgi et al. 2018, Super et al. 2018, Steinthorsdottir et al. 2021a). Most recent atmospheric CO_2 reconstructions reveal a broad range of ~400–600 ppm during the MCO, with transient peak values up to 800 ppm (Kürschner et al. 2008; Beerling et al. 2009, Foster et al. 2012, Zhang et al. 2013, Ji et al. 2018, Sosdian et al. 2018, Super et al. 2018, Stoll et al. 2019, Cui et al. 2020, Steinthorsdottir et al. 2021b). Consequently, the MCO is of particular interest since such conditions are broadly in line with future projections, depending on greenhouse gas emission-scenarios and climate sensitivity (Burke et al. 2018, Steinthorsdottir et al. 2021a). Moreover, geographical boundary conditions and a glaciated Antarctic continent make the Miocene a useful analogue in addition to the much warmer Early Eocene or the relatively less warm mid Pliocene Warm Period. The MCO has therefore been termed a suitable *'intermediate deep-time climate analogue'* (Burke et al. 2018, Steinthorsdottir et al. 2021a).

Until recently, much research has focused on Early to Middle Miocene climates, but this mostly addressed high- and mid-latitude regions and deep ocean conditions (Shevenell et al. 2004, Pälike et al. 2006, Holbourn et al. 2007, Holbourn et al. 2015, Warny et al. 2009, Passchier et al. 2011, Tian et al. 2013, Herbert et al. 2016, Liebrand et al. 2016, Sangiorgi et al. 2018, Sangiorgi et al. 2021, Super et al. 2018, Super et al. 2020). However, the tropical band is a fundamental endmember for the global climate as it co-defines equator-to-pole temperature gradients and drives ocean-atmosphere circulation, global and monsoonal hydrological cycling and associated weathering intensity. Consequently, the tropics play a crucial part in ocean nutrient supply and carbon cycling. Here, we aim to evaluate the potential of a unique tropical marine sequence recovered at eastern equatorial Atlantic Ocean Drilling Program (ODP) Site 959 with a near-complete Early to Middle Miocene sedimentary record.

1.2. Benthic foraminiferal stable carbon and oxygen isotope signals

Equatorial Pacific benthic foraminiferral $\delta^{18}O$ variability during the Miocene Climatic Optimum was strongly paced by eccentricity-modulated precession (Holbourn et al. 2007, Holbourn et al. 2015), with the lowest $\delta^{18}O$ values when Earth reached perihelion in January during high eccentricity, corresponding to minimal, albeit dynamic (eastern) Antarctic ice volume and an ice-free Northern Hemisphere (Warny et al. 2009, Fielding et al. 2011, de Vleeschouwer et al. 2017, Sangiorgi et al. 2018, Bradshaw et al. 2021). In addition, Early to Middle Miocene obliquity-paced $\delta^{18}O$ and stable carbon isotope ($\delta^{13}C$) variability, which has been ascribed to high latitude ice volume dynamics, was strong during intervals associated with long-term (~2.4 Myr) eccentricity minima that coincide with long-term (~1.2 Myr) obliquity maxima (Pälike et al. 2006, Holbourn et al. 2013, Liebrand et al. 2016, Levy et al. 2019, Drury et al. 2021). Recent compilations of global mean sea level change across the MCO based on Pacific Ocean benthic foraminiferal $\delta^{18}O$ and Mg/Ca records suggest episodes of near ice-free conditions paced by eccentricity and climatic precession (de Vleeschouwer et al. 2017, Miller et al. 2020). As ice volume and extent increased during

the MMCT, Antarctic Ice Sheet (AIS) variability became increasingly sensitive to obliquity (e. g. Holbourn et al. 2005, Levy et al. 2019, Bradshaw et al. 2021).

The MCO is associated with a ~3.2 Myr-long (~16.7–13.5 Ma), ~0.6‰ positive $\delta^{13}C$ excursion of the global exogenic carbon pool, referred to as the Monterey Excursion (ME) (Vincent and Berger 1985, Holbourn et al. 2007). The ME is characterized by six carbon isotope maxima events (CM-events), representing ~400 kyr long eccentricity cycles modulated by long ~2.4 Myr cycles (Woodruff and Savin 1991, Holbourn et al. 2007, Liebrand et al. 2011, Sosdian et al. 2020). The ME has been interpreted as a long-term negative feedback process representing increased organic carbon burial (Vincent and Berger 1985, Woodruff and Savin 1991), mitigating long-term atmospheric CO_2 increase. Several mechanisms have been proposed to account for this enhanced organic carbon deposition (Vincent and Berger 1985, Raymo 1994, Sosdian et al. 2020), which seems counterintuitively associated with warming on orbital timescales. Hypotheses include increased volcanic degassing associated with the Columbia River Basalt Flood volcanism (CRBF) which facilitated sustained warming, or dynamics related to sea level, weathering and organic carbon burial along continental margins (Hodell and Woodruff 1994, Kasbohm and Schoene 2018, Sangiorgi et al. 2021). On eccentricity timescales, Sosdian et al. (2020) showed that the CM-events, corresponding to ~400 kyr eccentricity minima, represent positive feedback mechanisms during which surface ocean dissolved inorganic carbon and atmospheric pCO_2 decreased during relatively cool conditions. Eccentricity maxima mark reduced- or near ice-free conditions including a transient phase of apparent warming at 15.6 Ma (*peak warming*, Holbourn et al. 2015, Kochhann et al. 2016, Miller et al. 2020).

1.3. Research aim

The tropical marine record at ODP Site 959 offers an Early to Middle Miocene sedimentary record which can be analyzed with both carbonate-based and organic matter-based proxies. The sedimentary sequence was recovered close to the equator (latitude 3°37.70′N and longitude 2°44.10′W), roughly ~120 km offshore of Ivory Coast (Fig. 1b). Neogene sediments dominantly comprise marine biogenic components, notably siliceous and carbonate microfossils, suitable for biostratigraphic and paleoceanographic studies, including calcareous nannofossils, diatoms, foraminifers and some clay (Mascle et al. 1996, Shafik et al. 1998, Norris et al. 1998a, b, Wagner 2002, van der Weijst et al. 2020, Weijst et al. 2022a). Initial studies also indicated the presence of organic matter (Wagner 2002), and its usefulness for stratigraphic and paleoclimatic purposes, including dinoflagellate cysts (Oboh-Ikuenobe et al. 1999). More recent work has shown the organic matter to include biomarker and dinoflagellate cyst assemblages suitable for paleoenvironmental reconstructions for portions of the Cenozoic (Awad and Oboh-Ikuenobe 2018, Awad and Oboh-Ikuenobe 2019, Frieling et al. 2018, Frieling et al.2019, Cramwinckel et al. 2018, Cramwinckel et al. 2019, Van der Weijst et al. 2022b).

Unfortunately, not much work has been carried out at the recovered lower to middle Miocene section since the shipboard analyses (Mascle et al. 1996, Norris 1998a, Shafik et al. 1998, Oboh-Ikuenobe et al. 1999, Wagner 2002, Awad and Oboh-Ikuenobe 2018, Awad and Oboh-Ikuenobe 2019). Consequently, this paper aims to produce a revised age model of the interval, the missing factor for high-resolution paleoclimate analyses at ODP Site 959. To this end, we first aim to establish a detailed bio-chemostratigraphy across the lead-up, onset and first 2 million years of the Miocene Climatic Optimum. This includes new calcareous nannofossil and diatom biostratigraphic data. Moreover, we generate bulk carbonate stable carbon and oxygen isotope ($\delta^{13}C$, $\delta^{18}O$) data to assess correlations to existing stratigraphies. These records, as well as high-resolution records of magnetic susceptibility and quantitative elemental composition are used to assess orbital cyclicity within the Milankovitch bands, to then tune the record to astronomical target curves and solutions. This sets the stage for follow-up reconstructions of Early to Middle Miocene climate variability recorded in pelagic sediments in the eastern equatorial Atlantic.

2. Materials

Sediments at Site 959 in the eastern equatorial Atlantic were recovered during ODP Leg 159 on a platform north of the Côte d'Ivoire-Ghana Marginal Ridge and on the southern edge of the Deep Ivorian Basin (3°37.659' N, 2°44.112' W, Fig. 1b; Mascle et al. 1996). Holes 959A-D were drilled at ~2100 m below sea level. At ~17 Ma, marine sedimentation occurred at a paleolatitude of ~1°S (±2.5°) based on paleolatitude.

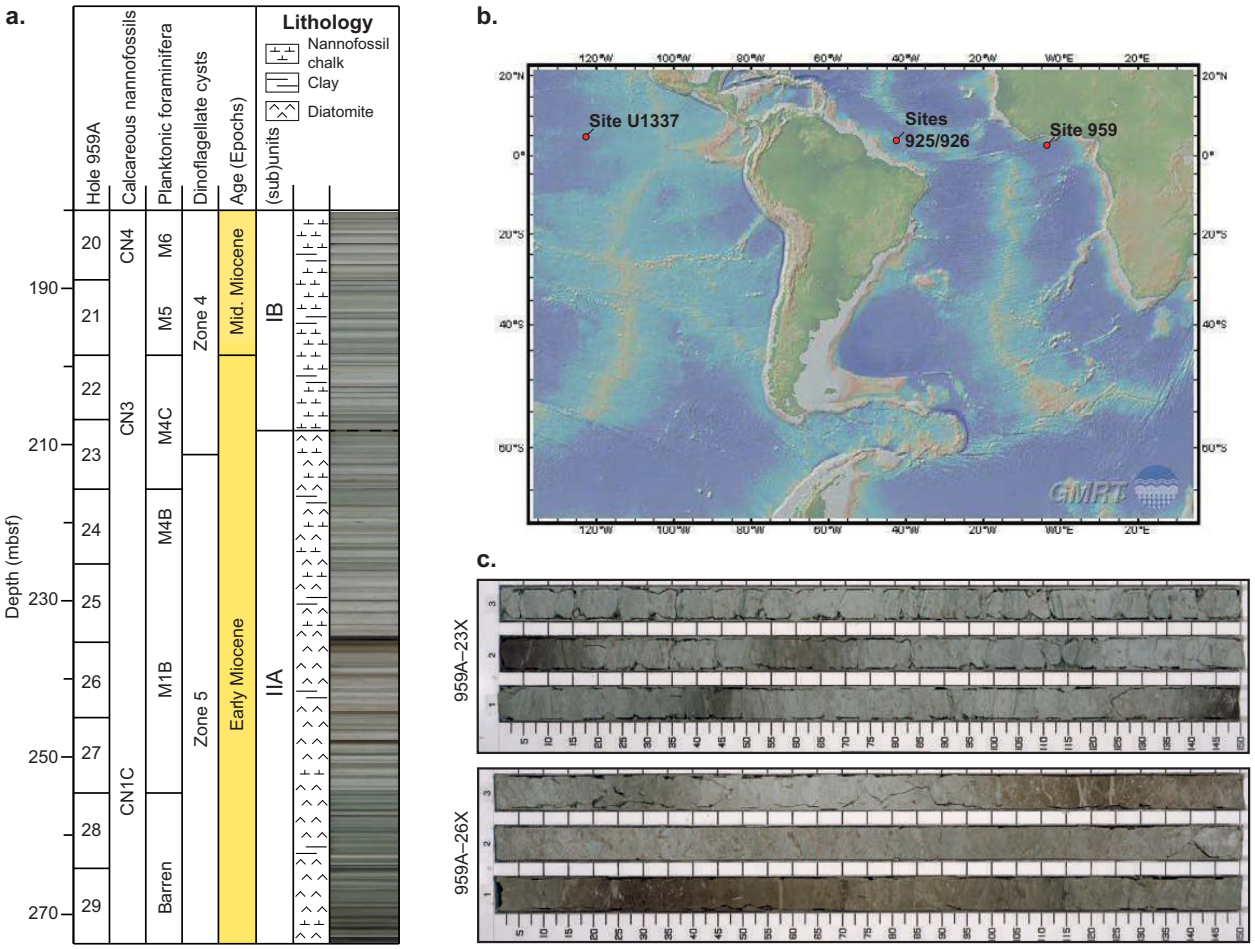

Fig. 1. a) Stratigraphic column of Early to Middle Miocene sediments recovered at ODP Hole 959A. Shipboard post-cruise calcareous nannofossil (Shafik et al. 1998), planktonic foraminifer (Norris 1998a) and dinoflagellate cyst (Oboh-Ikuenobe et al. 1999) biostratigraphy and lithostratigraphy (Mascle et al. 1996). The core image is generated by manually stacking core photographs. b) Map showing present-day locations of ODP Site 959, IODP Site U1337 and ODP Site 925/926 (generated with Global Multi-Resolution Topography (GMRT) v4.0; Ryan et al. 2009). c) Selected core photographs from Cores 23X (top) and 26X (bottom) showing the typical lithological variability (see Section 2).

org (version 2.1; van Hinsbergen et al. 2015), and paleomagnetic reference frame of Torsvik et al. (2012). Sediments are dominated by biogenic carbonate and silica, with subordinate clay and organic matter (Mascle et al. 1996, Wagner 2002). According to shipboard and subsequent post-cruise age assessment based on calcareous nannofossil- and planktonic foraminifer biostratigraphy, Hole 959A yields a presumably complete Early to Middle Miocene succession in Cores 29X-21X (Fig. 1a) (Mascle et al. 1996, Norris et al. 1998a, Shafik et al. 1998). However, even though core recovery is high (~103 %), the construction of a detailed age model and analyses of sedimentation history was hampered by the sparse presence of age-diagnostic microfossil taxa, including dinoflagellate cysts, calcareous nannofossils, planktonic foraminifera and silicoflagellates (Norris 1998a, Shafik et al. 1998, Schellpeper and Watkins 1998, Oboh-Ikuenobe et al. 1999).

The Miocene interval analyzed for this study is divided into two lithological Subunits IB and IIA (Fig. 1a; Mascle et al. 1996). Based on shipboard calcareous nannofossil and planktonic foraminifer biostratigraphy (Norris et al. 1998a, Shafik et al. 1998), these units comprise the lower to middle Miocene. Subunit IB (212.5–189.1 meters below sea floor (mbsf); 23X-4–21X, 40 cm) consists of clayey nannofossil chalk and clay with a relatively low

abundance of foraminifera (<5 %). On a cm-dm scale, alternations of light and dark layers occur which represent increased nannofossil abundance and increased clay levels, respectively (Fig. 1c, Mascle et al. 1996). Bioturbation is apparent throughout these alternations. The base of Subunit IB (212.5 mbsf; 23X-4, 40 cm) is defined by the first downhole occurrence of biogenic silica and diatoms as a major biogenic component (Mascle et al. 1996). Subunit IIA consists of diatom nannofossil chalk which progressively grades downhole into a clayey diatomite in the upper Oligocene (Mascle et al. 1996). The interval of interest in Subunit IIA (274–212.5 mbsf, 29X-CC–23X-4, 40 cm) is characterized by varying relative abundances of nannofossils and diatoms which manifest in alternating light and dark lithologies at 10–80 cm thickness (Fig. 1c). Sediments dominated by diatoms represent the darker phases (dark grey, brown and black) while increased clay and/or calcareous components correlate to lighter lithologies (light grey and light brown) (Mascle et al. 1996). Throughout Subunit IIA, pyrite is a common mineral phase and bioturbation is apparent, especially at lithological transitions.

Initial interpretation of the depositional setting based on microfossil assemblages implied an open marine setting (Mascle et al. 1996, Norris et al. 1998a). Upper Miocene sedimentary patterns at Site 959 have been interpreted to represent African monsoon-related climate variability at eccentricity timescales, which forced the recorded variability (Vallé et al. 2017). Cyclical variations in diatom abundance recorded in the lower Miocene were hypothesized to reflect monsoon variability forced by higher nutrient availability derived from enhanced upwelling of deeper waters (Mascle et al. 1996, Wagner 2002). More specifically, initial shipboard silicoflagellate analyses demonstrated two striking high-productivity events, one directly before the Oligocene-Miocene transition and one during the latest Early Miocene (Mascle et al. 1996, Schellpeper and Watkins 1998). The deposition of organic carbon-rich diatomites in the lower Miocene interval indicates enhanced organic carbon preservation (Wagner 2002). It is argued that this is linked to highly productive conditions and relatively low oxygen levels, which were likely associated with upwelling of nutrient-enriched deeper waters, paced by monsoon-related cyclical fluctuations (Wagner 2002). Moreover, increased occurrence of siliceous microfossils, coinciding with low relative abundances of terrestrial organic matter and higher sedimentation rates, correlate to apparent cyclical distribution of increased peridinioid organic walled dinoflagellate cysts relative to gonyaulacoids, indicative of increased productivity (Oboh-Ikuenobe et al. 1999). Collectively, this evidence points to a relatively productive open ocean environment with variations in nutrient supply through upwelling and/or fluvial nutrient supply, both in the Milankovitch band through monsoon variability and on longer time scales.

3. Methods

3.1. Depth scale

The lower and middle Miocene was recovered only in Hole 959A (Mascle et al. 1996). Therefore, despite optimal core recovery, gaps in the recovered record are almost certainly present between the cores. Vallé et al. (2017) constructed a spliced composite depth scale of the upper Miocene to lower Pleistocene cores from Holes 959A (9H–3H), 959B (11H–3H) and 959C (11H–4H), based on Fe intensities from XRF-scans. Cyclic patterns in the depth scale were subsequently tuned to eccentricity in the orbital solution of La2004 (Laskar et al. 2004). To allow for correlation of the Fe record between cores, Vallé et al. (2017) initially added constant offsets to the mbsf depth scale for each core to correct for variable expansion between holes and >100 % recovery. Based on similar considerations, we initially assumed an average core gap of 0.5 m for Cores 28X to 21X. Therefore, we converted the original mbsf scale to a revised mbsf scale by adding 0.5 m to each individual core, from here on referred to as rmbsf (supplementary Table T1).

3.2. Sampling and sample handling

Samples were collected at the Bremen Core Repository from the working halves of cores between 280.22 and 207.76 rmbsf (28X-1, 94 cm to 21X-1, 1 cm). We continuously sampled for half round samples at a 2 cm resolution which has left the sections depleted. During sampling, drilling mud and caved material was avoided. All samples were freeze-dried and possible remaining contamination along the rims of samples was removed in the GeoLab at Utrecht University. We subsequently generated lithological, biostratigraphic and geochemical data, which are all included in the supplementary information (Tables T2–T8).

3.3. Magnetic susceptibility

Magnetic susceptibility (MS) represents the abundance of magnetizable material in sediments, which is measured by subjecting the sample to an external magnetic field (Ellwood et al. 2000). High MS indicates the relative dominance of ferromagnetic and paramagnetic components (i. e., magnetite, Fe-rich clays) compared to a lower abundance of diamagnetic components (i. e., carbonates and SiO_2). In the interval between 280.22 and 207.99 rmbsf (28X-1, 94 cm–21X-1, 23 cm), freeze-dried samples were selected at an average resolution of 4 cm (n=2080), coarsely crushed, and then stored in pre-weighed plastic vials and subsequently measured for mass-normalized magnetic susceptibility (magnetic susceptibility relative to mass; '*X*' $m^3\ g^{-1}$) on a multifunction Kappabridge (MFK1-FA) connected to the Safyr data acquisition software at Paleomagnetic Laboratory Fort Hoofddijk, Utrecht University. Single samples were measured multiple times to determine repeatability (average s. d. = 0.06 *10^8 $m^3\ g^{-1}$).

3.4. Bulk carbonate stable isotope ratios

Bulk carbonate oxygen ($\delta^{18}O$) and stable carbon ($\delta^{13}C$) isotope ratios were measured in the interval between 280.22 and 206.78 rmbsf (28X-1, 94 cm–21X-1W, 1 cm) at an average resolution of 6 cm (n=1326). Freeze-dried sediment was powdered and approximately ~200-300 µg was weighed and transferred to 10 ml Na-glass vials. Sealed vials were flushed with helium and samples were converted to gaseous CO_2 by addition of 100 % orthophosphoric acid (H_3PO_4) using a ThermoFinnigan Gasbench-II, which was subsequently led on a helium flow to a Thermo Delta V Isotope Ratio Mass Spectrometer (IRMS). Correction for drift and regression, and conversion of isotope ratios relative to the Vienna Pee Dee Belemnite (‰VPDB) was carried out using 11 in-house standards (NAXOS) and 4 international standards (IAEA-CO-1) interspersed in every run of 60 samples. External precision, or reproducibility, is ~0.07‰ for carbon and ~0.08‰ for oxygen.

3.5. Color analysis

We assess if lithological variability in the section, reflected in the sediment color, provides information on Milankovitch cyclicity. Shipboard color reflectance redness versus greenness (a*), yellowness versus blueness (b*) and lightness (L*) were generated on cores 28X–23X at 5 cm resolution (Mascle et al. 1996). However, due to intense bioturbation especially at lithological transitions, sediment color changes are often obscured at this resolution. Therefore, we generate new sediment color data, i. e., mean greyscale (GS), blueness (b), greenness (g) and redness (r), based on drilling core images of archive-halves by applying the 'DeCrack' MatLab algorithm (Zeeden et al. 2015). Prior to color analyses, bioturbation and other color changes not related to the lithology visible in the core photos were removed by making them black. Data were generated at 1 cm intervals between 280.22–206.78 rmbsf (28X-1, 94 cm–21X-1, 1 cm) (n=6753). The threshold value for crack recognition was set at 65 and the percentage of dark and/or cracked pixels to exclude at 80 %.

3.6. ICP-OES elemental analyses

Quantitative elemental composition was determined with Inductively Coupled Plasma – Optical Emission Spectrometry (ICP-OES; Perkin Elmer Avio 500) at Utrecht University at an average resolution of 16 cm (n=459). To this end, ~100–125 mg freeze-dried and powdered material was dissolved in 2.5 ml HF and 2.5 ml $HClO_4/HNO_3$ (2:3) mixture in a closed Teflon container and stored on a 90 °C hot plate overnight. Subsequently, samples were reheated to 140 °C to form a gel which was then re-dissolved in 1M HNO_3 at 90 °C during a second night. Eventually, ~6 ml of the solution was transferred to 15 ml Greiner tubes for analysis. The average accuracy (recovery) of Ca was between 97–109 % and average analytical uncertainty 1 %, based on in-house standards, duplicates and an internal Germanium standard.

An approximation of weight percentage (wt%) $CaCO_3$ is determined based on the linear relationship between ICP-OES derived Ca concentrations (ppm) and previously published low resolution wt% $CaCO_3$ data spanning the complete study interval (supplementary Fig. S1) (Wagner 2002). Assuming that all Ca is part of the carbonate fraction (i. e., 0 % $CaCO_3$ at 0 ppm measured Ca concentrations), this linear regression was forced through zero (r^2 = 0.94).

3.7. Biostratigraphy

For analysis of calcareous nannofossil biohorizons, smear slides were prepared at an average resolution of 40 cm throughout the sampled interval. Biohorizons

were identified based on a calcareous nannofossil biostratigraphic framework of the Miocene through Pleistocene (Backman et al. 2012). In Backman et al. (2012), age estimates of biohorizons were derived from astronomically tuned cyclostratigraphies, mostly from ODP Site 925 and 926 in the tropical western Atlantic Ocean (Ceara Rise; Pälike et al. 2006), which we converted to the GTS2020 timescale (Gradstein et al. 2020, Raffi 2020).

Secondly, diatom biostratigraphy was established by identifying diatom events previously reported in Pälike et al. (2010) for IODP Expedition 320/321, Pacific Equatorial Age Transect (PEAT, Pälike et al. 2010). The ages reported in Pälike et al. (2010) are based on diatom biochronology from the central Pacific (DSDP Sites 572 and 575; Barron 1985) and the eastern equatorial Pacific (DSDP Sites 71, 77 and 495; Barron 1983). These ages were subsequently converted to GTS2020 (Gradstein et al. 2020). The average resolution of samples examined for diatom biostratigraphy was ~40 cm.

3.8. Spectral analysis

Spectral analysis was performed by using the Acycle software package (Li et al. 2019). Prior to analyses, proxy records were linearly resampled to their individual median sampling resolution and detrended with the local weighted regression smoothing (LOWESS) algorithm. Subsequently, periodicity was determined by applying the multitaper method (MTM) in the depth domain with 2π taper (Thomson 1982) and by generating fast Fourier transform evolutive spectra (Kodama and Hinnov 2015). Confidence levels were acquired based on the Robust Red Noise model (AR1, Gilman et al. 1963) with spectral peaks deemed reliable if exceeding the 95 % confidence level.

4. Results

4.1. Mean greyscale

The mean GS record shows a high degree of correspondence with the core photographs. After visual comparison to the photographs, 21 datapoints with anomalously low values were removed from the record. The record – and the photographs – shows decimeter and meter-scale variability (Fig. 2b). Importantly, as previously reported (Wilkens et al. 2017), the 1.5 m and 10–11 m scale variability are likely the result of uneven lighting during core photography, which introduces artificial variability corresponding to section length (~1.5 m) and core length (~10–11 m).

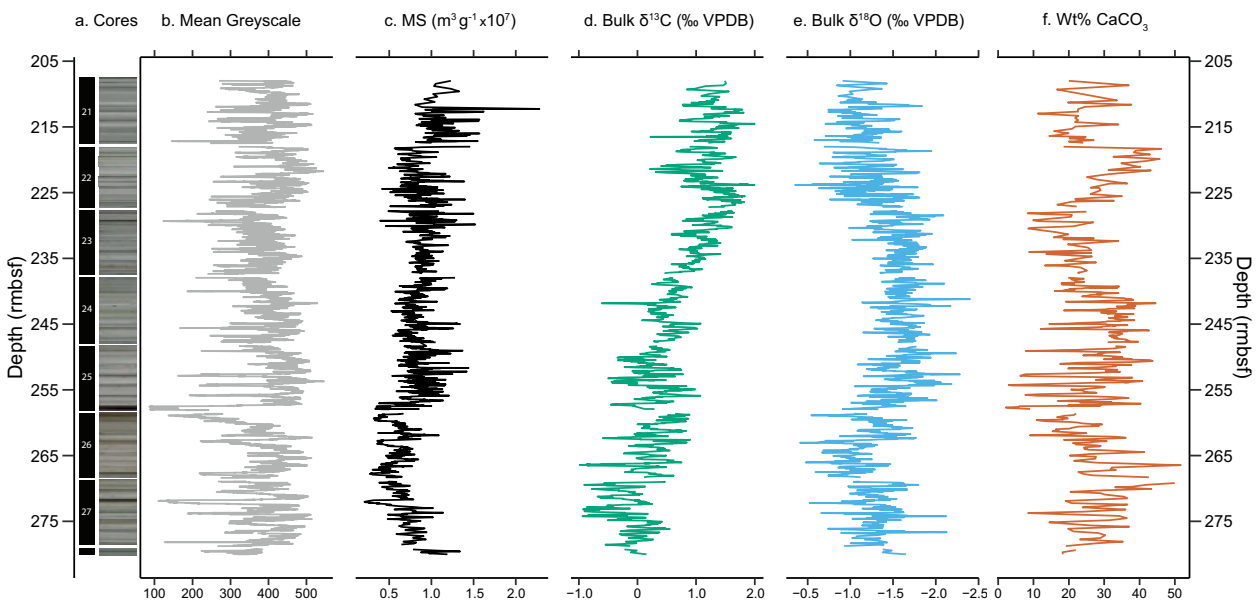

Fig. 2. Overview of proxy data generated from ODP Site 959. a) Core photos (Mascle et al. 1996). b) Mean greyscale. c) Bulk sediment magnetic susceptibility (MS). d) Bulk carbonate $\delta^{13}C$. e) Bulk carbonate $\delta^{18}O$. f) Estimated wt% $CaCO_3$. Gaps in the records reflect core gaps incorporated in the rmbsf depth scale.

Here, we take a core length that is longer than reported by ODP (~9.6–9.8 m) due to the addition of 0.5 m per core for construction of our revised depth scale. Between ~280 and 258 rmbsf, color variability is characterized by dark, relatively broad intervals and amplitude variability is comparably high. The broad dark intervals also correlate to peaks in redness (a* and redness/greenness ratio) and greenness/blueness ratio (supplementary Fig. S2, S3). Subsequently, between 258 and 250 rmbsf, high amplitude, meter-to-sub-meter alternation of black and light grey intervals characterize the GS record. Herein, darkest lithologies also correspond to peaks in greenness/blueness ratio (supplementary Fig. S2, S3). Between 250 and 205 rmbsf, amplitude variability is generally lower, and, on average colors remain relatively light.

4.2. Magnetic Susceptibility

The MS has an increasing trend throughout the record, with stepped increases at 258 rmbsf and at 217 rmbsf, both signifying an abrupt increase in terrigenous material (Fig. 2c). Below 258 rmbsf, meter-scale variability is characterized by high amplitude (2.5–11 * 10^{-7} m^3g^{-1}), broad MS minima which are spaced 5–12 meters apart. In this interval, MS exhibits a visible positive correlation with GS, which indicates a correlation to relatively less dark, i. e., light brown, colors (low GS) (Fig. 3c). Simultaneously, there is no clear relation with wt% $CaCO_3$ (Fig. 3f). Above the first abrupt increase at 258 rmbsf, MS variability is characterized by decimeter-to-meter-scale variability with especially high amplitude between 254 and 247 rmbsf, and from 231 to 223 rmbsf. Above the second abrupt increase at 217 rmbsf, similar short-scale variability continues, punctuated by a striking maximum at 212.26 rmbsf (2.2 *10^{-7} m^3g^{-1}). Throughout this interval (~254–207.99 rmbsf), high MS values generally correspond to low wt% $CaCO_3$ ($p < 0.0001$, $r^2 = 0.27$; Fig. 3e), while there is no clear relation with GS (Fig. 3b).

4.3. $CaCO_3$ weight percentages

Weight percentages of $CaCO_3$ range between ~0.7 % and 51.7 % and vary on ~20–30 m scale throughout the record (Fig. 2f). Between 265 and 258 rmbsf, wt% $CaCO_3$ decreases from an average of 40 % to <5 %, followed by an abrupt increase of ~25 %. Immediately above this, the record is characterized by pronounced (±20 %), meter-scale variability with especially striking decreases between 258 and 240 rmbsf. Between 220 and 218 rmbsf, a broad peak (~46 %) is recorded, followed by an abrupt crash to ~15 % at 218.01 rmbsf. Especially between 280 and 258 rmbsf, high wt% $CaCO_3$ values generally correlate to bulk carbonate $\delta^{13}C$ minima ($p < 0.0001$, $r^2 = 0.38$; Fig. 3i).

4.4. Bulk carbonate stable isotope ratios

Reliable isotope ratios were determined for all 1326 samples. However, samples with wt% $CaCO_3$ <5 % between 257.91 and 257.4 rmbsf (Fig. 2f) are likely significantly biased by authigenic carbonate formations and we therefore exclude bulk carbonate isotope ratios within this interval from further analyses.

We record a ~1‰ rise in bulk carbonate $\delta^{13}C$ values between 250 and 225 rmbsf from average values of ~0.5‰ to average values of ~1.5‰ (Fig. 2d). Between 280 and 250 rmbsf, the $\delta^{13}C$ record is characterized by high amplitude (~1.5‰), meter-scale variability, including prominent minima spaced approximately 3–4 meters apart (274.1, 269.45, 266.08, 262.35, 257.26, 253.24 and 250.1 rmbsf). Between 250–208 rmbsf, $\delta^{13}C$ minima are less pronounced, but they seem to occur on 2-meter to sub-meter scales. A striking minimum at 221.42 rmbsf interrupts the relatively constant trend in this interval.

The long-term trend in the bulk carbonate $\delta^{18}O$ record at Site 959 is characterized by decreased absolute values (~-1.6‰) and decreased amplitude variability between 257.37 and 227.2 rmbsf, following background values of ~-1.2‰ in the lower part of the record (280–258 rmbsf; Fig. 2e). Above 227 rmbsf, values increase again to ~-1.2‰ and remain relatively constant in the upper part of the record (207.99 rmbsf). Meter-scale variability characterizes the $\delta^{18}O$ record, with especially striking minima between 227 and 207.99 rmbsf.

Throughout the studied interval, there seems to be good correspondence between meter-scale variability in the bulk carbonate $\delta^{13}C$ and $\delta^{18}O$ records (Fig. 3j–l), with $\delta^{13}C$ minima corresponding to $\delta^{18}O$ minima, albeit with a different slope between ~280–258 rmbsf ($p < 0.0001$, $r^2 = 0.26$), relative to the interval between ~258–208 rmbsf ($p < 0.0001$, $r^2 = 0.3$).

4.5. Biostratigraphy

New calcareous nannofossil and diatom biostratigraphic data generated for this study lead to robust, initial age constraints which confirm that the studied

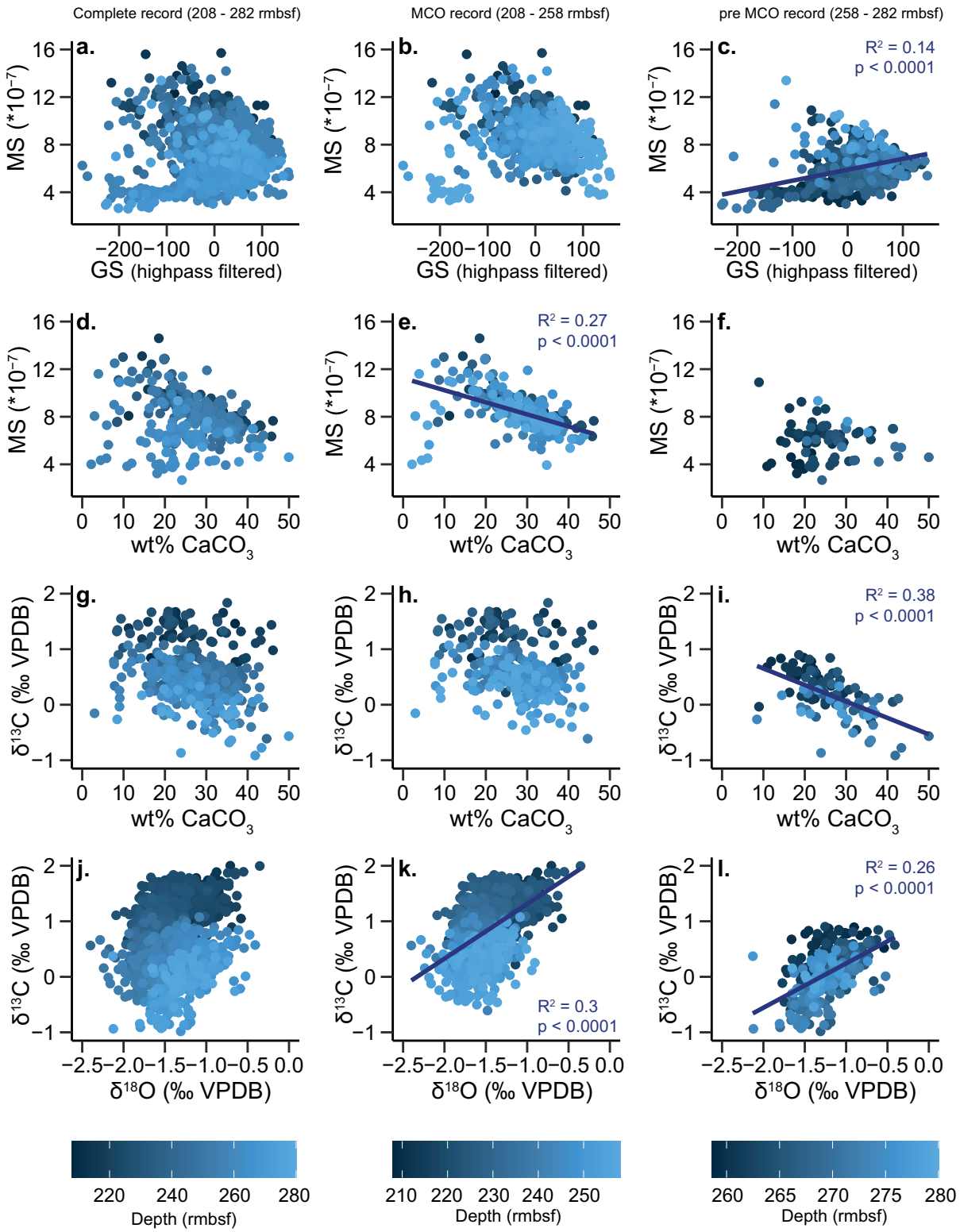

Fig. 3. Selected cross plots of Site 959 proxy records. The shade of blue represents the depth of the data points (see scale). Left column includes the complete datasets (a, d, g, j), the middle column includes data in the interval between 208 to 258 rmbsf (b, e, h, k) and the right column includes data from the interval between 258 to 280 rmbsf (c, f, i, l). Solid blue lines represent linear regression models with associated coefficient (R^2) and probability (p).

Table 1. Biostratigraphic age tie-points used in this study. Calcareous nannofossil ages are based on those reported in Backman et al. (2012). Diatom ages are reported according to the chronology reported in Pälike et al. (2010) and subsequently converted to GTS2020 (Gradstein et al. 2020). Notes: T = Top occurrence, B = Bottom occurrence.

Type	Event	Age GTS2020 (Ma)	Average depth (rmbsf)	Core-Section, Interval (Top)	Core-Section, Interval (Bottom)
Calcareous nannofossils	T *Helicopshaera ampliaperta*	14.86	207.23 ±0.76	20X-6, 145–147 cm	21X-1, 23–25 cm
	T common *Discoaster deflandrei*	15.8	226.39 ±0.4	22X-6, 48–50 cm	22X-6, 88–90 cm
	B *Discoaster signus*	15.85	227.5 ±0.3	22X-7, 69–71 cm	23X-1, 0–2 cm
	B *common Sphenolithus heteromorphus*	<17.65	257.4 ±0.2	25X-6, 136–138 cm	25X-7, 25–27 cm
	T *Sphenolithus belemnos*	17.94	269.4 ±0.4	27X-1, 6–8 cm	27X-2, 15–17 cm
Diatoms	T *Rhaphidodiscus marylandicus*	16.49	243 ±0.2	24X-4, 40–42 cm	24X-4, 80–82 cm
	B *Annellus californicus*	16.99	256.8 ±0.4	25X-6, 58–60 cm	25X-6, 136–138 cm
	B *Craspedodiscus coscinodiscus*	16.99	256.8 ±0.4	25X-6, 58–60 cm	25X-6, 136–138 cm
	T *Craspedodiscus elegans*	18.18	288.04 ±0.34	28X-6, 93–95 cm	28X-7, 10–12 cm
	B *Nitzschia maleinterpretaria*	18.27	288.49 ±0.11	28X-7, 10–12 cm	28X-7, 33–35 cm
	B *Triceratium pileus*	18.27	288.49 ±0.11	28X-7, 10–12 cm	28X-7, 33–35 cm

interval spans the Early to Middle Miocene (Table 1; Fig. 4, S4–S6) (Norris 1998a, Shafik et al. 1998). Firstly, the Top (T) *Helicosphaera ampliaperta* (14.86 Ma; Backman et al. 2012) event is found at 207.23 ±0.76 rmbsf. At 226.39 ±0.4 rmbsf, the T common occurrence of *Discoaster deflandrei* is identified (15.8 Ma; Backman et al. 2012). Immediately preceding this occurrence, the base (B) of *Discoaster signus* is identified at 227.5 ±0.3 rmbsf, which marks the boundary between Miocene biozones CNM6 and CNM7 during the Early Langhian (15.85 Ma; Backman et al. 2012). Furthermore, at 257.4 ±0.2 rmbsf, common *Sphenolithus heteromorphus* specimens are found which suggests proximity to the lower occurrence of the marker (B c *S. heteromorphus*), which marks the boundary between biozones CNM5 and CNM6 at 17.65 Ma (Backman et al. 2012). At 269.4 ±0.4 rmbsf, T *Sphenolithus belemnos* is identified (17.94 Ma), preceded by B *S. belemnos* at 284.6 rmbsf (19.01 Ma), which marks the boundary between biozones CNM4 and CNM5 (Backman et al. 2012).

Calcareous nannofossils become diluted by an increasing number of diatoms and clay below ~270 rmbsf. However, the presence of rare *Sphenolithus delphix* in a single sample at 351.05 rmbsf, interspersed by rich diatom assemblages, indicates a stratigraphic position close to the Oligocene-Miocene transition at 23.11 Ma (Backman et al. 2012). Within the Lower Miocene interval (~280–258 rmbsf) of this study, diatom datums also provide further age constraints. Some diatom zonal markers reported from the equatorial Pacific were found to be extremely rare at Site 959 (e. g., *Nitzschia maleinterpretaria*, *Rhaphidodiscus marylandicus*), and some were not observed at all (*Thalassiosira praefraga*, *T. spumellaroides*, *T. primalabiata*). B *Annellus californicus* and B *Craspedodiscus coscinodiscus* are identified at 256.8 ±0.4 rmbsf. In the equatorial Pacific, these events are isochronous at 16.99 Ma, and together they indicate that this interval falls within subzone A of *Crucidenticula nicobarica* Diatom Zone, spanning 17.49–16.15 Ma on the PEAT time scale (Barron 1985, Pälike et al. 2010). At 288.04 ±0.34 rmbsf, T *Craspedodiscus elegans* event was identified which is assigned an age of 18.18 Ma in the equatorial Pacific (Barron 1985, Pälike et al. 2010). Furthermore, two isochronous diatom events were identified at 288.49 ±0.11 rmbsf (B *Nitzschia maleinterpretaria* and B *Triceratium pileus*). In the equatorial Pacific cores, both these events are assigned an age of 18.27 Ma (Barron 1983, Pälike et al. 2010).

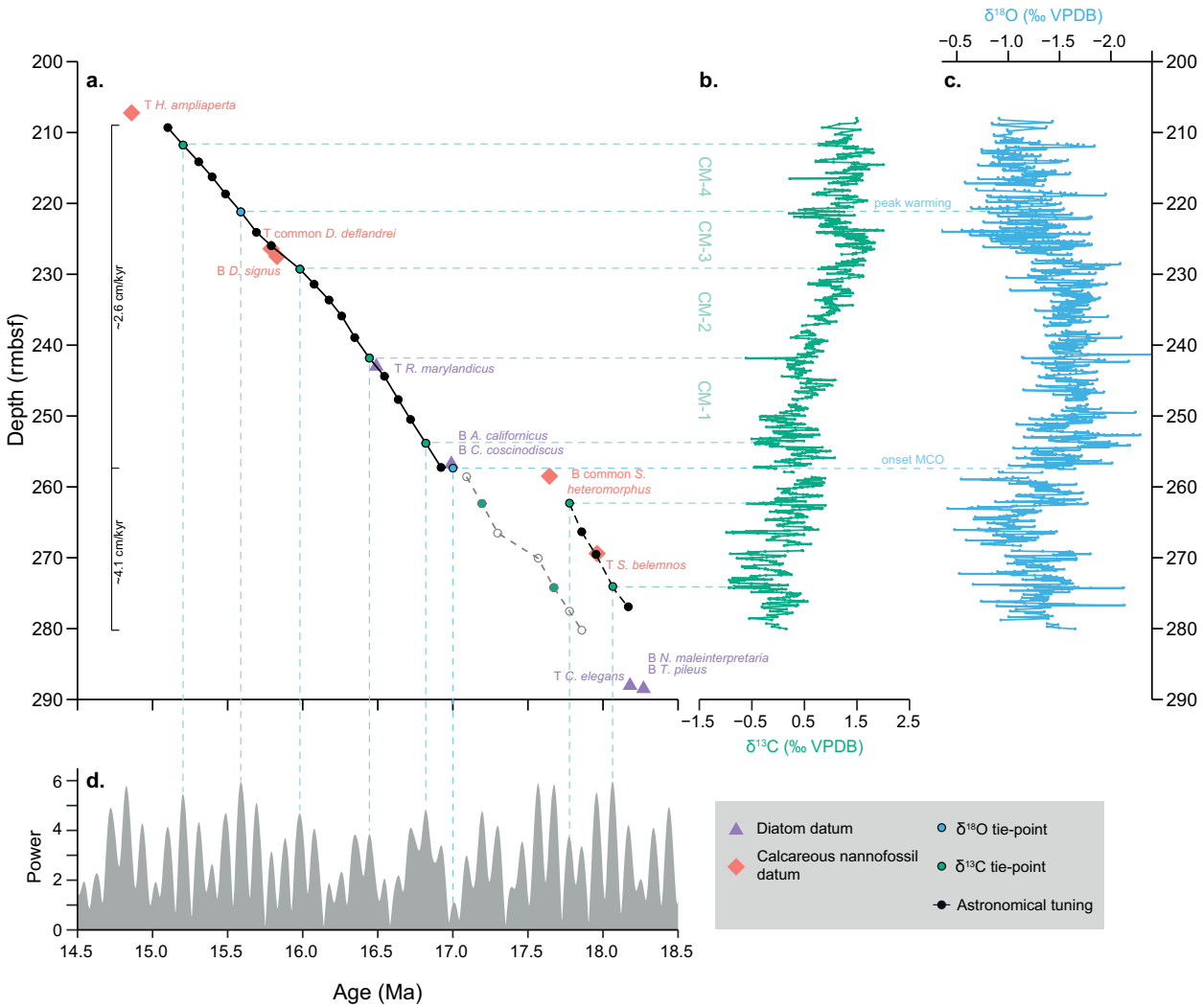

Fig. 4. Site 959 isotope stratigraphy and correlation to eccentricity extracted from the Laskar et al. (2004) orbital solution. a) Age-depth model including biostratigraphic tie-points (peach diamonds and purple triangles) and tuning tie-points (black dots) based on $\delta^{13}C$ events (green dots) and $\delta^{18}O$ events (blue). Dashed black and grey lines indicate the two tuning options for the pre-MCO interval according to calcareous nannofossil (black) or diatom biostratigraphy (grey) (see Section 5.2.2). Average linear sedimentation rate is indicated next to the vertical depth scale. b) Bulk carbonate $\delta^{13}C$. c) Bulk carbonate $\delta^{18}O$. d) Eccentricity extracted from the Laskar et al. (2004) orbital solution. Green dashed lines represent correlation of low $\delta^{13}C$ values to ~400 kyr maxima. Blue dashed lines represent correlation of *peak warming* and the onset of the MCO, as recorded in the bulk carbonate $\delta^{18}O$ record, to eccentricity. CM-# = Carbon Maxima events.

5. Integrated stratigraphy

5.1. Bulk carbonate isotope stratigraphy and bio-chemostratigraphic framework

Using the diatom and calcareous nannofossil biostratigraphy, we can identify several chemostratigraphic markers that provide initial age constraints for the lower and middle Miocene at Site 959 (Fig. 4). A significant decrease of ~0.5‰ reported in the bulk carbonate $\delta^{18}O$ record at 258 rmbsf likely reflects the warming associated with the onset of the MCO at ~16.9 Ma (Fig. 4c). Subsequently, we infer that the prominent increase in bulk carbonate $\delta^{13}C$ between 250 and 225 rmbsf (~0.5‰ to 1.5‰) represents the Monterey Excursion (Fig. 4b). Immediately prior to the onset of the ME (~245–240 rmbsf), a short lasting decrease in $\delta^{13}C$ values to ~0‰ is recorded, reminiscent of the ~200 kyr-long carbon cycle perturbation

shown in deep ocean benthic foraminiferal $\delta^{13}C$ records from the Pacific Ocean at ~16.9 Ma (Holbourn et al. 2015). Moreover, pronounced $\delta^{13}C$ decreases at 230.84, 241.83, 221.42 and 211.77 rmbsf likely reflect CM-events 1, 2, 3 and 4 (Holbourn et al. 2007) (Fig. 4c). CM-3 has previously been associated with MCO *peak warming* at 15.6 Ma (Holbourn et al. 2014, Holbourn et al. 2015), but at Site 959 this event corresponds to relatively negative, albeit not strikingly low, $\delta^{18}O$ values (~-1.7‰; Fig. 4b).

The age model shows that trends and changes in MS, wt% $CaCO_3$ and mean GS records consistently correspond to the onset of the MCO, the Monterey Excursion, and the MCO *peak warming* event (Fig. 2, 4). For example, the $\delta^{18}O$ decrease at ~258 rmbsf characterizes the onset of the MCO and occurs simultaneously with a steep rise in MS and immediately follows a striking dark (low mean GS), and $CaCO_3$-depleted interval (Fig. 2). Furthermore, the *peak warming* event, signified in the $\delta^{13}C$ record by a prominent decrease at ~221.42 rmbsf, correlates to a light lithological interval (high GS) with high wt% $CaCO_3$ values and relatively low $\delta^{18}O$ values (Fig. 2). However, significant discrepancies between the various biostratigraphic events remain between ~280–250 rmbsf. In this interval, diatoms suggest ages consistently somewhat younger than calcareous nannofossils (Fig. 4a, S4, Table 1).

5.2. Cyclostratigraphy

5.2.1. Evolutive and spectral analyses

Cyclic variability in the bulk carbonate $\delta^{13}C$, $\delta^{18}O$, wt % $CaCO_3$ and MS records was tested by evolutive and spectral analyses in the depth domain. Given the clear overprint of lighting cycles in the color data (see section 4.1), the mean GS record was not used for testing cyclicity. Spectral analyses reveal high-amplitude cycles with frequencies between ~12.5–10 m, ~3.5–2.5 m, ~1.5–1 m, and ~0.65–0.45 m (Fig. 5), of which average periods increase with depth implying a decreasing sedimentation rate. These observations reveal frequencies with a ratio of approximately 1:2.5:10:20, which suggests significant influence of astronomical climate forcing by long and short eccentricity, obliquity and precession. Hence, we attribute the ~12.5–10 m cyclicity to reflect long eccentricity (~400 kyr), the ~3.5–2.5 m cycles to correspond to short eccentricity (~100 kyr), the ~1.5–1 m to obliquity (~41 kyr) and the ~0.65–0.45 m to precession (~23–19 kyr). This implies sedimentation rates of ~3.5–2.5 cm/kyr, consistent with estimates from our newly generated diatom biostratigraphy and chemostratigraphic results.

Gaussian bandpass filters were applied to filter the ~12.5–10 m cycle (0.083 ±0.02 cycle/m) from the MS, $\delta^{13}C$ and wt% $CaCO_3$ power spectra. These reveal that during 400 kyr eccentricity-related minima in MS and $\delta^{13}C$, coinciding with a maximum in wt% $CaCO_3$, there is increasingly clear representation of variability in the precession band (Fig. 6). This is also visible in the $\delta^{18}O$ record. This modulation is especially apparent in all proxy records during MCO peak warming (grey band; Fig. 6). We interpret this as eccentricity modulation of precession, supporting our interpretation of the spectral output. In addition, it further supports the notion that minima in the MS and $\delta^{13}C$ and maxima in wt% $CaCO_3$ represent maxima in orbital eccentricity.

Continuous evolutive spectral analyses show that low frequency periods are more dominant in the $\delta^{13}C$ and wt% $CaCO_3$ records, while shorter cycles are relatively better represented in the MS and $\delta^{18}O$ records (Fig. 5). This is consistent with the long eccentricity pacing of the Early Miocene carbon cycle (Pälike et al. 2006, Holbourn et al. 2007, Holbourn et al. 2015, Liebrand et al. 2016, Beddow et al. 2018).

5.2.2. Astronomical tuning with the bulk carbonate $\delta^{13}C$ record

To improve the initial temporal framework, we tuned the bulk carbonate $\delta^{13}C$ record to the La2004 orbital solution (Laskar et al. 2004) (Fig. 7). The $\delta^{13}C$ was selected for its clear expression of the ~400 kyr and ~100 kyr cycles. Even though we consider that the $\delta^{13}C$ record could respond to astronomical forcing in a non-linear fashion, the deep ocean carbon isotope record has been shown to represent variability in the global exogenic carbon pool, which should be represented in the bulk carbonate $\delta^{13}C$ record at Site 959 as well. Despite the fact that the sampling resolution of all proxy records, except for wt% $CaCO_3$, allows for analysis on precession- to obliquity timescales, we used the extracted eccentricity component as a tuning target. This approach was chosen since higher frequency cycles show more irregularities in the evolutive spectra of the depth-series (Fig. 5). Furthermore, by tuning to eccentricity, we avoid introducing uncertainty related to the stability of precession and obliquity due to minimal constraints on tidal dissipa-

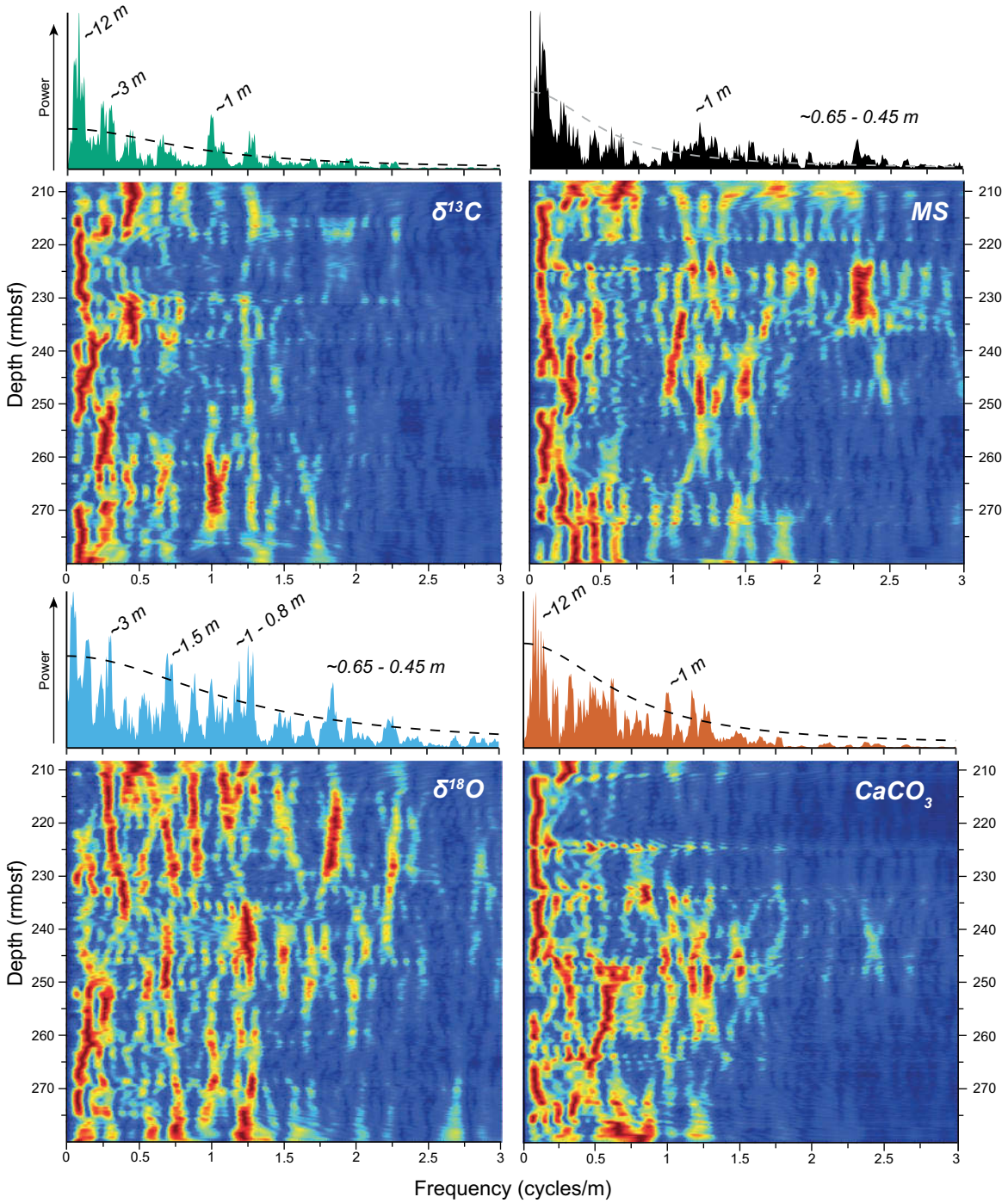

Fig. 5. Power and evolutive spectra of bulk carbonate $\delta^{13}C$ (left top), MS (right top), bulk carbonate $\delta^{18}O$ (left bottom) and wt% $CaCO_3$ (right bottom) records from Site 959 against depth (rmbsf). 95 % confidence level is depicted in dashed lines and most notable cycles are indicated in the power spectra.

tion and dynamical ellipticity beyond 10 Ma (Hüsing et al. 2007, Zeeden et al. 2014). Tuning was carried out by correlating orbital extremes in selected proxy records to long (~400 kyr) and short (~100 kyr) eccentricity (Fig. 7). To this end, we use a maximum of 1 tie-point per ~100 kyr cycle to avoid introducing artificial periodicity, without assuming a lag between the tuning target and proxy data. Tuning was anchored at the peak

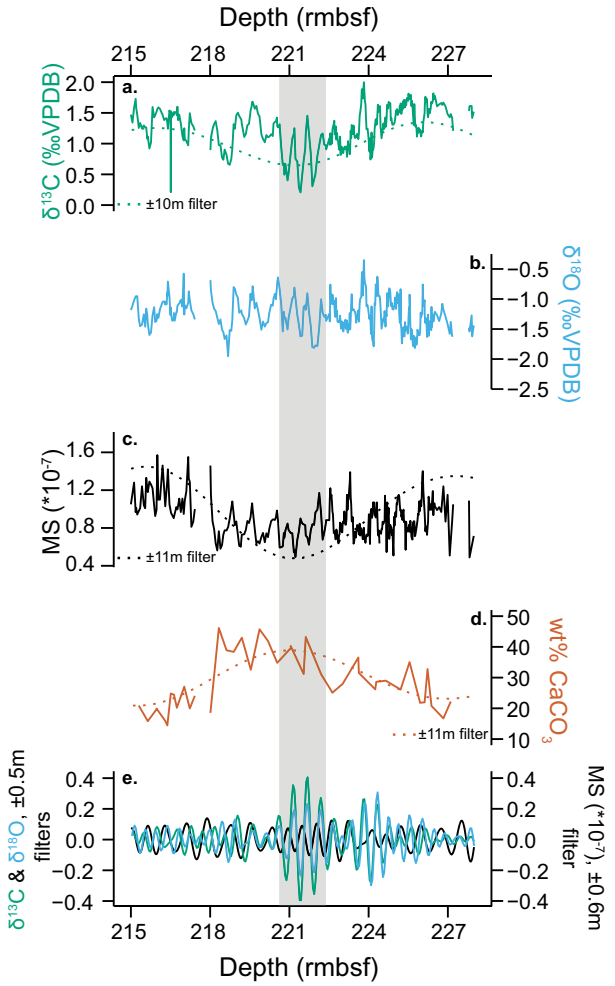

Fig. 6. ~400 kyr amplitude modulation of precession during *peak warming* at ~15.6 Ma in the Site 959 record (vertical grey bar). a) Bulk carbonate $\delta^{13}C$ record and Gaussian filtered ±10 m cycle, interpreted as 400 kyr eccentricity. b) Bulk carbonate $\delta^{18}O$. c) MS and Gaussian filtered ±11 m cycle, interpreted as 400 kyr eccentricity. d) Estimated wt% $CaCO_3$ and Gaussian filtered ±11 m cycle, interpreted as 400 kyr eccentricity. e) Guassian filtered ±0.5 m cycles of the bulk carbonate $\delta^{13}C$ (green), $\delta^{18}O$ (blue) and MS (black) records showing clear, increased amplitude between ~223–220 rmbsf.

warming event at 221.42 rmbsf (~15.6 Ma) and the onset of the MCO identified at ~258 rmbsf (~16.9 Ma; Holbourn et al. 2015) (Fig. 4).

Recognition of long and short eccentricity cycles, indicated by most pronounced $\delta^{13}C$ minima is unambiguous for the interval between 257.5 and 207.7 rmbsf. Correlation was aided by recognition of CM-events and by visual comparison to previously published $\delta^{13}C$ records covering the Early- Middle Miocene (Holbourn et al. 2007, Holbourn et al. 2015, Kochhann et al. 2016, Sosdian et al. 2018), which supports our interpretation of the ~12 m cycles as ~400 kyr eccentricity cycles in this interval. Throughout this interval, $\delta^{13}C$ minima correlate to MS and $\delta^{18}O$ minima and to wt% $CaCO_3$ maxima. Following the known phase relation of $\delta^{18}O$ and $\delta^{13}C$ with eccentricity (Pälike et al. 2006, Holbourn et al. 2007, Holbourn et al. 2015, Liebrand et al. 2016), we tuned (most pronounced) $\delta^{13}C$ minima to ~400 kyr and ~100 kyr eccentricity maxima (Fig. 7). Consequently, almost 5 long eccentricity cycles are recognized, covering CM-events 1–4 (~16.9 –15.09 Ma), and 19 short eccentricity cycles are counted, which implies an average sedimentation rate of ~2.6 cm/kyr. Between Cores 22X and 23X, a gap is inferred due to an absent, but expected, short-eccentricity cycle, while the other core gaps do not cover significant missing time.

Based on recognition of pronounced $\delta^{13}C$ minima in the interval prior to the onset of the MCO (280.22–258.63 rmbsf), five ~100 kyr eccentricity maxima could be confidently identified (Fig. 7). However, significant discrepancy between biostratigraphic tie-points in this interval complicates confident astronomical tuning (Fig. 4). Considering the calcareous nannofossil bio-events, the presence of common and continuous *S. hetermorphus* specimens at 257.4 ±0.2 rmbsf implies an age of <17.65 Ma just prior to the onset of the MCO, as identified by the isotope stratigraphy. Together with preceding calcareous nannofossil biohorizons at 269.4 ±0.4 rmbsf (T *S. belemnos*, 17.94 Ma) and at 284.6 rmbsf (B *S. belemnos*, 19.01 Ma), a similar sedimentation rate is determined as inferred from diatom biohorizons in the same interval, though continuously offset to younger ages (Fig. 4). Following the calcareous nannofossil biohorizons, this implies a hiatus of maximally ~700 kyr just prior to the onset of the MCO. However, this hiatus is likely shorter given that the true B *S. heteromorphus* event was not found in Core 26X and is likely located in the gap between 25X and 26X (Fig. 4a). In contrast, diatom events indicate that the interval just prior to the onset of the MCO has an age of 16.99 Ma (B *A. californicus* and B *C. coscinodiscus* at 256.8 ±0.4 rmbsf, Fig. 4, Fig. S7, Table 1). The mismatch between calcareous nannofossil- and diatom biostratigraphy could be related to paleobiogeographic differences between the equatorial Atlantic and Pacific Oceans, but due to limited diatom biostratigraphic data from reliably dated records in the equatorial Atlantic any possible diachroneity between Atlantic and Pacific

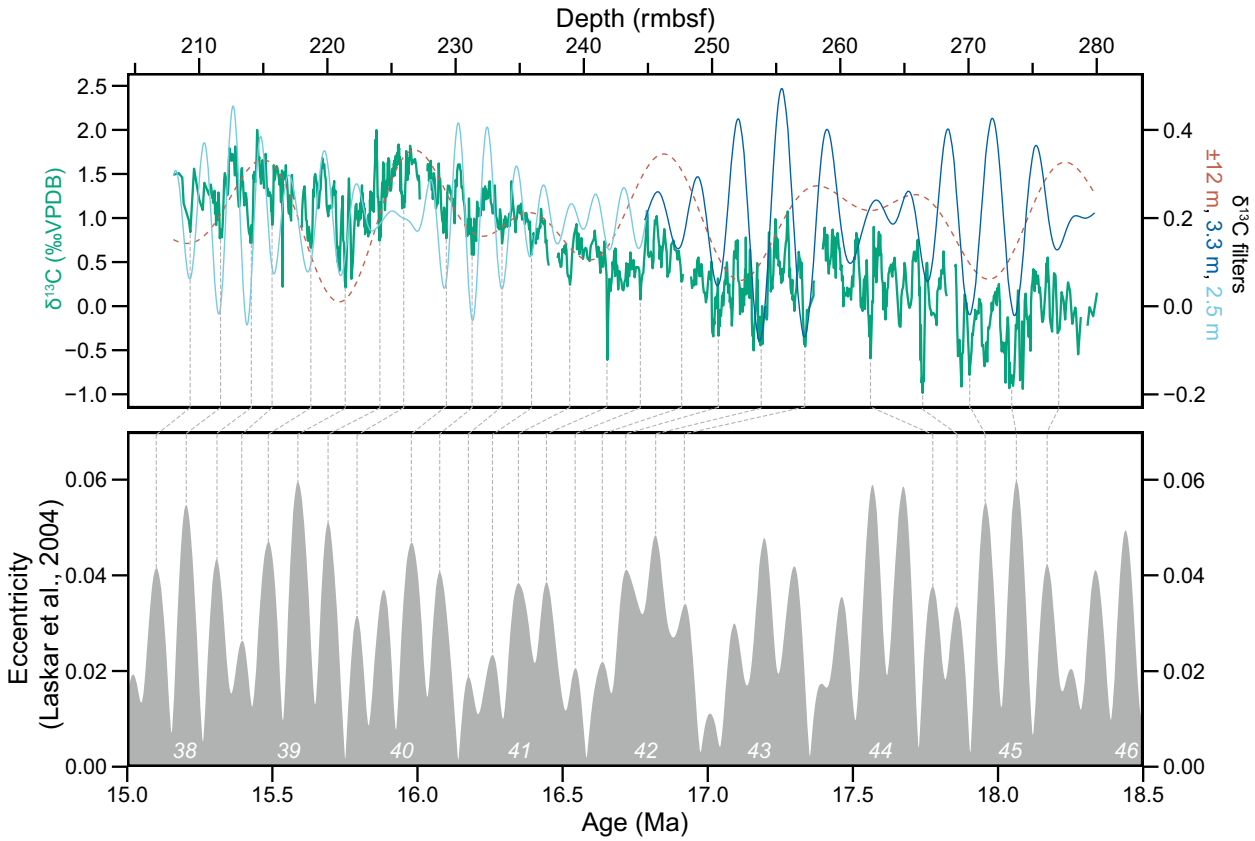

Fig. 7. Orbital tuning of the Site 959 bulk carbonate $\delta^{13}C$ record (green graph, upper panel) with Gaussian filtered ±12 m cycle (orange dashed line), interpreted as ~400 kyr eccentricity, and Gaussian filtered 3.3–2.5 m cycles (light and dark blue lines), interpreted as ~100 kyr eccentricity. Bottom panel shows eccentricity extracted from the orbital solution of Laskar et al. (2004). Numbers represent ~400 kyr eccentricity cycles as in Liebrand et al. (2016). Grey dashed lines represent tuning tie-points.

diatom datums remains difficult to test. On the other hand, calcareous nannofossil events at Site 959 correspond well to the previously reported calcareous nannofossil biostratigraphy in the western equatorial Atlantic (ODP Sites 925/926; Backman et al. 2012). Hence, we tune the pre-MCO interval at ODP Site 959 according to the calcareous nannofossil biohorizons (Fig. 4, 7).

Subsequently, we tuned the two striking, and equally negative, $\delta^{13}C$ minima at 269.45 and 274.1 rmbsf to the two ~100 kyr eccentricity maxima belonging to the 400 kyr eccentricity maximum at ~18.03 Ma (#45, Fig. 7). Furthermore, we infer a hiatus of maximally ~700 kyr in the gap between cores 25X and 26X, but the exact duration is most likely shorter given the uncertain placement of the B common of *S. heteromorphus* between Cores 25X and 26X. Alternatively, as the core gap falls between the dark, bio-siliceous sediment and the lighter sediments richer in carbonate, the record could also be continuous and contain a very condensed interval with significantly lower sedimentation rates. Condensed records at the onset of the MCO have been previously reported from other locations (Liebrand et al. 2016, Drury et al. 2021). However, loss of material between cores 25X and 26X is likely given the drilling device used (extended core barrel; XCB) and considering the more robust calcareous nannofossil biostratigraphy in this interval, we surmise a hiatus prior to the onset of the MCO at Site 959. The average linear sedimentation rate in the pre-MCO interval is ~4.08 cm/kyr and final tuning indicates that the studied interval spans ~18.2–15 Ma.

5.2.3. Analysis of tuned records

Using the age model derived from tuning of the $\delta^{13}C$ record to the extracted eccentricity from the La2004 solution, spectral analysis was carried on the complete

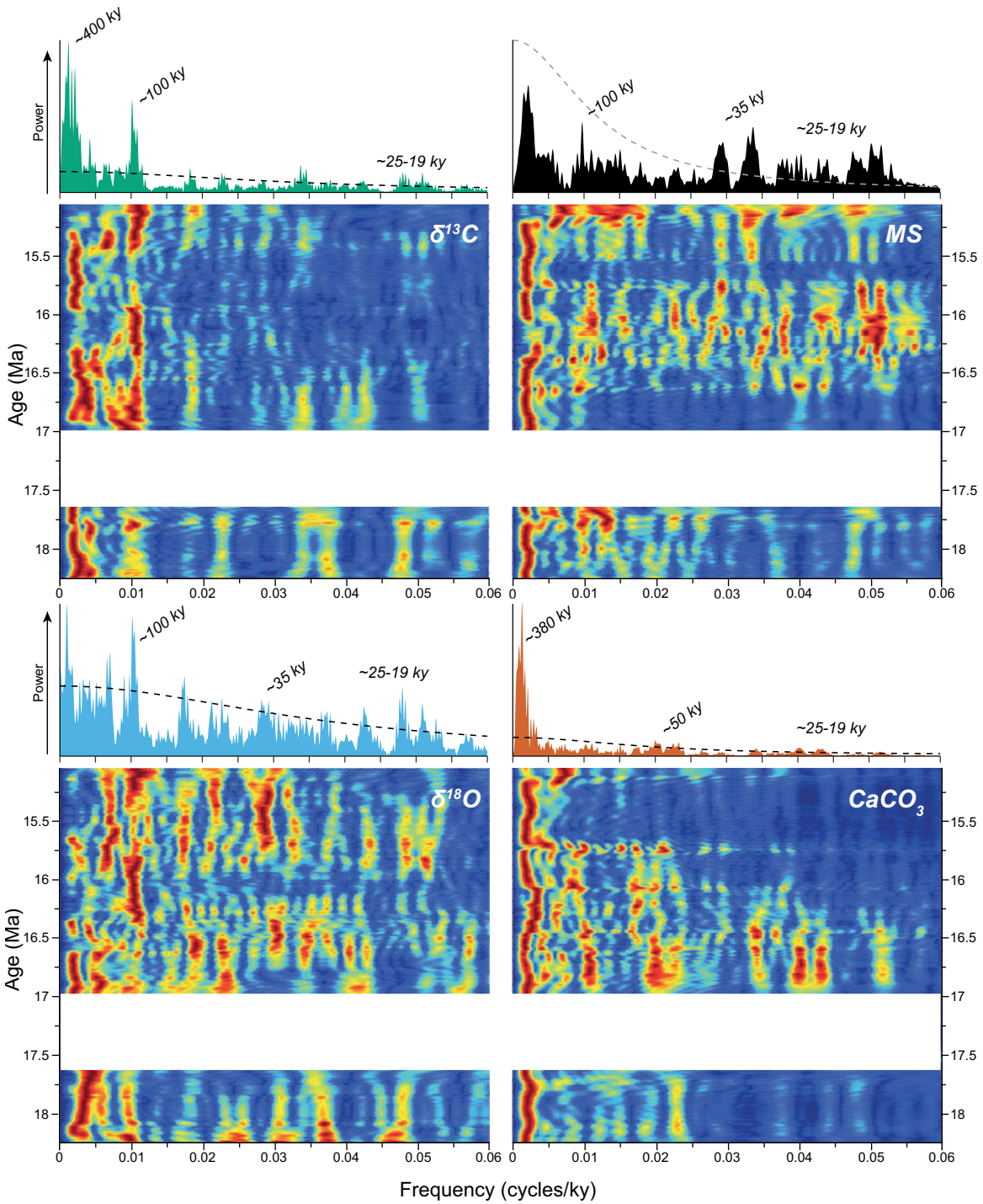

Fig. 8. Power and evolutive spectra of bulk carbonate $\delta^{13}C$ (left top), MS (right top), bulk carbonate $\delta^{18}O$ (left bottom) and wt% $CaCO_3$ (right bottom) records from Site 959 against age. In the interval of the hiatus (~17–17.6 Ma), spectral output is unreliable and therefore not shown. 95 % confidence level is depicted in dashed lines and most notable cycles are indicated in the power spectra.

records in the time-domain (Fig. 8). Power spectra of the $\delta^{13}C$ and wt% $CaCO_3$ reveal a significant broad peak centered at ~400 kyr. Its bandpass filter shows that this long eccentricity is particularly forced by the most negative $\delta^{13}C$ values and highest $CaCO_3$ percentages (Fig. 9f). On top of the $\delta^{13}C$ record, all other records reveal significant peak strength at ~100 kyr. Here, ~100 kyr eccentricity maxima correspond to

$\delta^{13}C$ and MS minima and $\delta^{18}O$ and wt% $CaCO_3$ maxima. The dominance of eccentricity in the $\delta^{13}C$ record is expected given the relatively long residence time of carbon (Pälike et al. 2006, Zeebe et al. 2017), but we also acknowledge that additional power could be induced given that the $\delta^{13}C$ record was used for tuning.

In addition to the clear eccentricity forcing, continuous evolutive spectra also show significant high (er) frequency forcing (Fig. 8). Analogous to previous work (Beddow et al. 2018), we find a prominent ~50 kyr cycle in the %$CaCO_3$ record within the interval following the onset of the MCO (~16.9–16 Ma) (Fig. 8), which corresponds to pronounced wt% $CaCO_3$ minima. In addition, we find strong expression of ~35 kyr cycles, especially prominent in the $\delta^{18}O$ and MS records during the MCO (~16.5–15 Ma). As hypothesized by Beddow et al. (2018), the ~50 kyr cycle could be related to the first harmonic of ~100 kyr eccentricity cycle, but both the ~50 kyr and ~35 kyr cycles could also be related to obliquity. To further elucidate these cycles, notably different from the main astronomical Milankovitch frequencies, more detailed analyses of the proxy records than presented here is required. Finally, in the $\delta^{18}O$ and MS records, and to a lesser extent in the $\delta^{13}C$ record, we find multiple cycles within the ~20–25 kyr frequency band, which we interpret to reflect precession forcing. Follow-up work will further interpret and test the significance of these higher frequency cycles.

6. Discussion

6.1. ODP Site 959 isotope stratigraphy and deep ocean records

Previous reconstructions of Early to Middle Miocene isotope stratigraphy have been largely based on benthic foraminiferal isotope ratios (Pälike et al. 2006, Holbourn et al. 2007, Holbourn et al. 2015, Liebrand et al. 2011, Liebrand et al. 2017). The bulk carbonate $\delta^{13}C$ and $\delta^{18}O$ record at Site 959 dominantly represents surface ocean-derived calcareous nannofossils (Mascle et al. 1996). Offsets of absolute isotopic values at Site 959 relative to benthic foraminifer records are therefore dominantly caused by higher temperatures and the fractionation effect of the biological pump. However, the major trends between our $\delta^{18}O$ and $\delta^{13}C$ records and the benthic foraminifer isotope records correspond well, especially considering orbital scale fluctuations (Fig. 10), indicating that they reflect variability of the global climate and the global exogenic carbon pool and that the signals are derived from primary calcite that is not too strongly affected by diagenesis.

6.1.1. Bulk carbonate $\delta^{18}O$ record

Our $\delta^{18}O$ record at Site 959 shows general resemblance to deep ocean benthic foraminiferal $\delta^{18}O$ records, including relatively low values during the MCO (Fig. 9). On orbital time scales, the lowest $\delta^{18}O$ values correspond to eccentricity maxima, like in the deep ocean records.

At ODP Site 959, the onset of the MCO is marked by a bulk carbonate $\delta^{18}O$ decrease of ~0.5‰ marking the warming associated with the Miocene Climatic Optimum (Lear et al. 2000, You et al. 2009, Sangiorgi et al. 2018, Sangiorgi et al. 2021, Super et al. 2018, Super et al. 2020, Fig. 9d). This excursion is only approximately half of that recorded in deep ocean benthic foraminiferal $\delta^{18}O$ records (Woodruff and Savin 1991, Billups et al. 2002, Holbourn et al. 2007, Holbourn et al. 2015, Kochhann et al. 2016, Fig. 10d). Presumably, the drop in $\delta^{18}O$ records is primarily a function of ice sheet melt and warming, with the melt of ice sheets affecting all records equally as it influences global ocean $\delta^{18}O$. Therefore, the 0.5‰ smaller excursion at Site 959 compared to the deep ocean records might indicate muted warming in tropical regions relative to high latitude surface waters that feed the deep ocean. Alternatively, a relative increase in local seawater $\delta^{18}O$ results from changes in local ocean-atmosphere circulation. Potentially the same explanation holds for our relatively muted signal at 15.6 Ma, referred to as *peak warming* in the benthic foraminifer record at Site U1337 in the Pacific (Holbourn et al. 2015, Kochhann et al. 2016). Interestingly, throughout the entire studied interval the variability in the Site 959 $\delta^{18}O$ record on long-eccentricity timescales is much smaller than that in the deep ocean benthic foraminifer records (Fig. 10, orange arrows). This could allude to polar amplification of temperature variability. However, this hypothesis requires further testing with more sophisticated proxies that only track temperature variability.

6.1.2. Bulk carbonate $\delta^{13}C$ record

Generally, the shape of the bulk carbonate $\delta^{13}C$ record strongly resembles that of the deep ocean benthic foraminifer records, including a clear Monterey Ex-

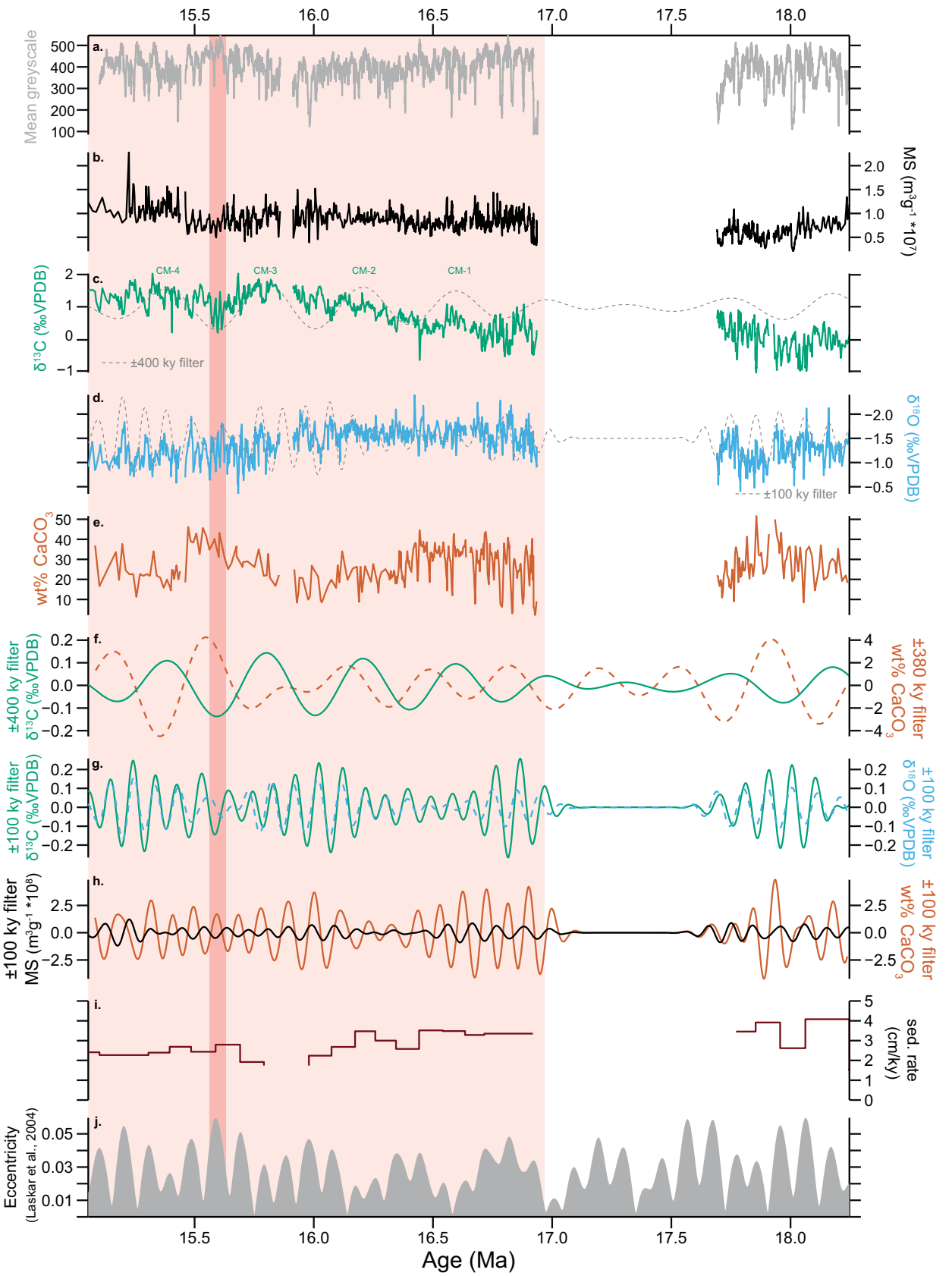
15.5
16.0
16.5
17.0
17.5
18.0
a.
Mean greyscale
500
400
300
200
100
b.
MS (m3g-1 *10-7)
2.0
1.5
1.0
0.5
c.
δ13C (‰VPDB)
CM-4
CM-3
CM-2
CM-1
±400 ky filter
d.
δ18O (‰VPDB)
±100 ky filter
e.
wt% CaCO3
f.
±400 ky filter δ13C (‰VPDB)
±380 ky filter wt% CaCO3
g.
±100 ky filter δ13C (‰VPDB)
±100 ky filter δ18O (‰VPDB)
h.
±100 ky filter MS (m3g-1 *10-8)
±100 ky filter wt% CaCO3
i.
sed. rate (cm/ky)
j.
Eccentricity (Laskar et al., 2004)
Age (Ma)

Fig. 9. Compilation of Site 959 proxy records (a–e), Gaussian filtered eccentricity cycles (f–h) and sedimentation rate (i) compared to eccentricity extracted from the Laskar et al. (2004) orbital solution (j). Light red area indicates the MCO as identified at Site 959 and the vertical red bar represents *peak warming* at ~15.6 Ma.

cursion, CM-events, and the transient $\delta^{13}C$ drop at 15.6 Ma (Fig. 9 and 10). This supports a defining influence of global exogenic $\delta^{13}C$ on our new record. However, several interesting differences occur. At Site U1337 in the deep equatorial Pacific (Fig. 1; Holbourn et al. 2015), the onset of MCO warming (~16.9 Ma) is associated with a small drop in benthic foraminiferal $\delta^{13}C$ (i. e., carbon cycle perturbation) which is followed by a sharp onset of the Monterey Excursion at ~16.7 Ma. In contrast to the equatorial Pacific $\delta^{13}C$ record, the onset of the MCO does not show a significant drop in $\delta^{13}C$ at Site 959 and there is not a sharp onset of the Monterey Excursion. Furthermore, we find relatively high wt% $CaCO_3$ at the onset of the MCO rather than pronounced carbonate dissolution as recorded in the deep Pacific (Fig. 10; Pälike et al. 2012, Holbourn et al. 2015). We ascribe these differences to the relatively shallow water depth at the drilling location of Site 959 compared to the eastern equatorial Pacific Site U1337. Consequently, shoaling of the carbonate compensation depth (CCD) during the so-called carbon cycle perturbation (Piela et al. 2012, Holbourn et al. 2015, Kochhann et al. 2016) would have had less influence on carbonate preservation at Site 959. Carbonate dissolution at the onset of the ME has been extensively covered in the equatorial Pacific (Pälike et al. 2012), but evidence is lacking for the low-latitude Atlantic Ocean.

6.2. Depositional variability at ODP Site 959

The MS, wt% $CaCO_3$ and mean greyscale records offer insight into the depositional setting at ODP Site 959. Here, these records mark the relative abundances of terrigenous material, at Site 959 represented by clays (magnetic susceptibility), carbonates (wt% $CaCO_3$) and biogenic silica (i. e., diatomites) which are likely forced by variability in West African monsoon circulation, consistent with previous Late Miocene and Pliocene records (e. g., Vallé et al. 2017). Although a direct measure of the abundance of biogenic silica is lacking, shipboard lithological descriptions indicate that darkest sediments are diatomaceous, while lighter sediments, i. e., lighter brown and/or (light) grey, indicate increased clay and/or calcareous components, respectively (Mascle et al. 1996, Wagner 2002). Furthermore, shipboard color reflectance b* (yellowness versus blueness; Mascle et al. 1996) data has previously been used as a proxy for diatom content at other locations (McKay et al. 2019).

Prior to the MCO (~18.2–17 Ma), diatomites characterize the depositional system, as shown by striking dark brown lithological intervals (Fig. 1) and relatively increased b* values (Fig. S2 and S3). Generally, the thickest diatomites were deposited during ~400 kyr eccentricity maxima, while short-scale variability in the color record seems to be forced by obliquity. Lowest MS values correlate to these dark lithological intervals, indicating a relative decline in terrigenous clay input, possibly reflecting a decrease in terrestrial sediment supply and/or continental weathering during these intervals. Alternatively, low MS values in this interval could be caused by dilution due to a relative increase in biogenic silica. Furthermore, we record a slight positive correlation between GS and MS (Fig. 3c), signifying that relatively lighter colors (i. e., light brown) correlate to higher clay abundances, compared to the black and darkest brown lithologies associated with diatomite layers. Assuming the dark diatomaceous layers represent increased primary productivity (Wagner 2002), enhanced nutrient supply would have been related to upwelling of nutrient-rich deeper waters rather than deriving from other sources, like fluvial input. This notion is supported by the negative correlation between $\delta^{18}O$ and GS (Fig. S8), implying that episodes of increased primary productivity are related to lower (or saltier) seawater temperatures, i. e., relatively high $\delta^{18}O$ values, consistent with upwelling of colder deep waters.

The onset of the MCO is associated with a major shift in the depositional setting and a change in variability. First, a visible positive relation between GS (and b*) and MS disappears (Fig. 3b, S2 and S3), as does the negative correlation between $\delta^{18}O$ and GS (Fig. S8). The abundance of $CaCO_3$ relative to biosiliceous components is much higher during the MCO, indicating a general shift in production from diatoms to coccolithophores, also shown by low average b* values after the MCO onset indicating decreased diatom content (Fig. S2, S3). In contrast to the interval prior to the MCO, the MCO is characterized by a

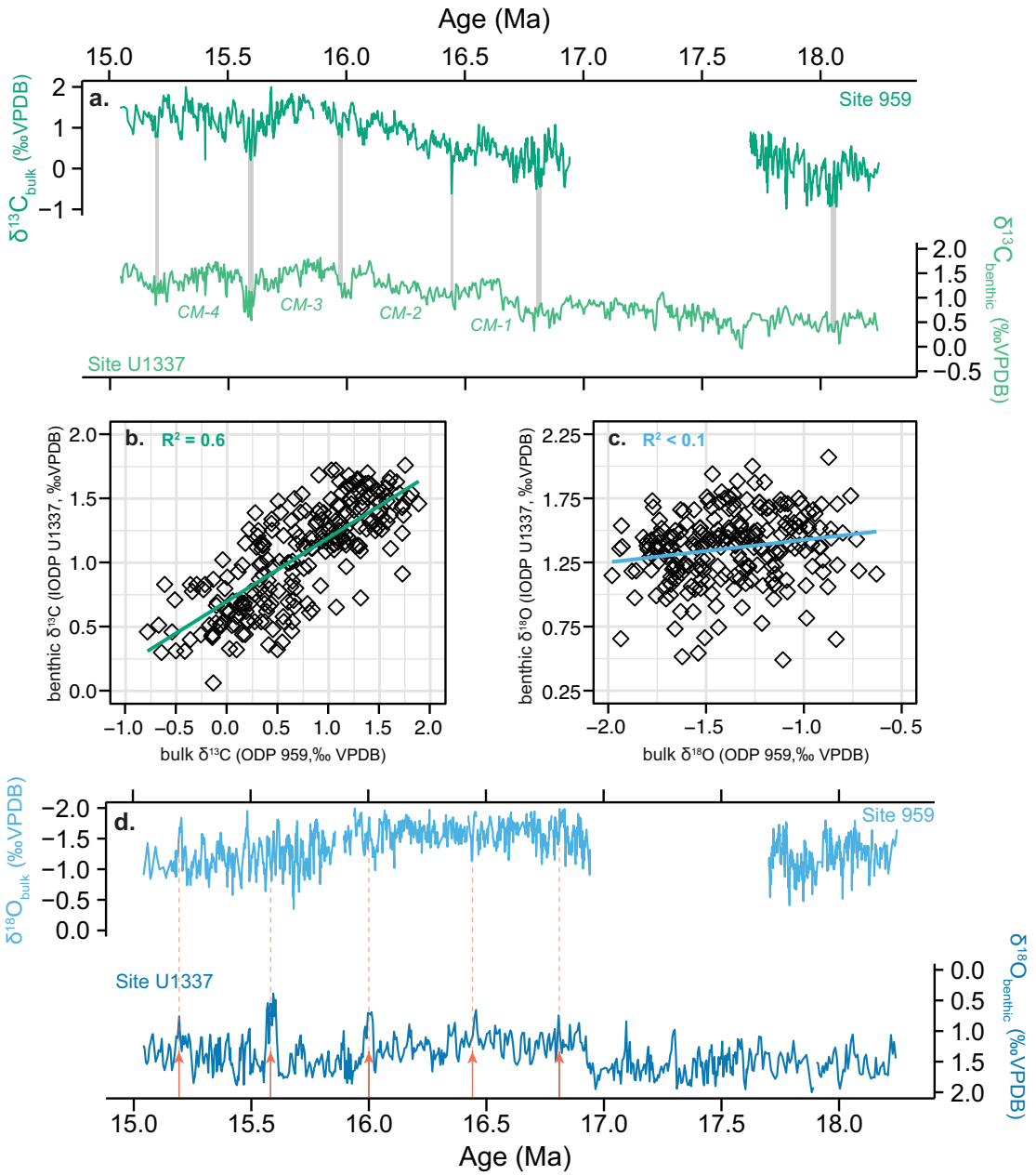

Fig. 10. ODP Site 959 isotope stratigraphy compared to the benthic foraminifer records from the equatorial Pacific, Site U1337 (Holbourn et al. 2015). a) Site 959 bulk carbonate $\delta^{13}C$ (dark green, top) and Site U1337 benthic foraminifer $\delta^{13}C$ (light green, bottom). Vertical grey bars indicate correlation of $\delta^{13}C$ minima and associated CM-events. b) Scatterplot of the benthic foraminifer versus bulk carbonate $\delta^{13}C$ records. Green line shows linear regression (R^2=0.61). c) Scatterplot of the benthic foraminifer versus bulk carbonate $\delta^{18}O$ records. Blue line shows linear regression (R^2<0.1). d) Site 959 bulk carbonate $\delta^{18}O$ (light blue, top) and Site U1337 benthic foraminifer $\delta^{18}O$ (dark blue, bottom). Orange arrows indicate ~400 kyr eccentricity maxima which show much higher amplitude in the benthic record compared to the bulk carbonate record of Site 959.

negative correlation between wt% $CaCO_3$ and MS (Fig. 3e, 9h). We surmise that this relation is rather determined by the variations in the degree of dilution of clays through variations in $CaCO_3$ production.

In contrast to dominantly 400 kyr forcing of diatomite deposition prior to the MCO, lithology varies on shorter orbital cycles during the MCO. Between ~16.9–16.6 Ma, immediately following the onset of

the MCO, high-amplitude alternations between diatomites and $CaCO_3$–rich deposits are expressed on 100 kyr time scales. Subsequently, between ~16.6–16.1 Ma, eccentricity-related amplitude variability in all records, but especially MS and $\delta^{18}O$, significantly decreases, which is also observed in spectra in the depth domain (~240–230 rmbsf; Fig. 5). This interval (~16.9–16.1 Ma) corresponds to a node in the ~2.4 Myr long eccentricity cycle, during which high-frequency cycles become increasingly dominant relative to eccentricity (Fig. 8). At ~16.0 Ma, directly following this node, the bio-siliceous sediment component disappears (Mascle et al. 1996), and eccentricity cycling becomes characterized by $CaCO_3$–rich lithologies during eccentricity maxima, which is especially prominent during the 400 kyr eccentricity maximum between ~15.7 and 15.5 Ma (Fig. 9).

7. Conclusions

Based on initial shipboard biostratigraphic age constraints and lithological analysis (Mascle et al. 1996, Norris et al. 1998a, Shafik et al. 1998, Wagner 2002), sediment cores retrieved at ODP Site 959 in the eastern equatorial Atlantic offer a unique tropical marine sequence, suitable for high-resolution bio-geochemical analysis. A robust age model was constructed based on newly generated biostratigraphic data and tuning the bulk carbonate $\delta^{13}C$ record to La2004-extracted eccentricity. The generated records span the interval from ~18.2 to 15 Ma, including a hiatus of maximally ~700 kyr just prior to the onset of the MCO. Similar to deep ocean benthic foraminiferal isotope ratios, climate and carbon cycle variability at Site 959 is dominantly forced by long- and short eccentricity, with shorter intervals of dominant obliquity forcing. The bulk carbonate isotope long term trends and events at ODP Site 959 are very similar to those in the benthic record of IODP Site U1337 in the eastern equatorial Pacific (Holbourn et al. 2015), including the Monterey Excursion and CM-events. Interestingly, the magnitude of negative $\delta^{18}O$ excursions at the onset of the MCO (~16.9 Ma) and *peak warming event* at ~15.6 Ma, as well as bulk carbonate $\delta^{18}O$ variability throughout the MCO, is subtler compared to benthic foraminiferal $\delta^{18}O$ records, which could allude to polar amplification of surface temperatures. Across the onset of the MCO, a lithological shift occurs from bio-siliceous dominated lithologies forced by eccentricity variability to $CaCO_3$–rich deposition on eccentricity to precession timescales, likely influenced by highly variable upwelling intensity. We conclude that the Lower to Middle Miocene records generated at Site 959 provide highly valuable opportunities for delving into the reconstruction of tropical marine temperature, productivity and depositional dynamics influenced by monsoonal-forced hydrological variability across the onset of the MCO.

Data availability: Depth conversion to rmbsf, calcareous nannofossil and diatom bioevents and range charts, MS, bulk carbonate isotopes, wt% $CaCO_3$ and color variability datasets of Site 959 are deposited at Zenodo https://doi.org/10.5281/zenodo.7584238

Acknowledgements. We thank the International Ocean Discovery Program and predecessors (notably the Ocean Drilling Program) for providing us with data and the samples analyzed in this study. This study is funded by the European Research Council Consolidator Grant 771497, awarded to AS, funded by the Horizon 2020 program. We also thank the Netherlands Earth System Science Centre (NESSC), financially supported by the Ministry of Education, Culture and Science (OCW), for fostering national collaborations. We are grateful for the technical support by Maxim Krasnoperov, Desmond Eefting, Arnold van Dijk and Coen Mulder (Utrecht University). We thank Adrianna Januszkiewicz and Amalia Notaro for help in processing samples, producing slides and analysis of diatom and calcareous nannofossil biostratigraphic examination.

References

Awad, W. K., & Oboh-Ikuenobe, F. E. (2018). Late Paleogene-early Neogene dinoflagellate cyst biostratigraphy of the eastern Equatorial Atlantic. *Journal of African Earth Sciences*, *140*, 267–281. https://doi.org/10.1016/j.jafrearsci.2018.01.014

Awad, W. K., & Oboh-Ikuenobe, F. E. (2019). Paleogene-early Neogene paleoenvironmental reconstruction based on palynological analysis of ODP Hole 959A, West Africa. *Marine Micropaleontology*, *148*, 29–45. https://doi.org/10.1016/j.marmicro.2019.03.003

Backman, J., Raffi, I., Rio, D., Fornaciari, E., & Pälike, H. (2012). Biozonation and biochronology of Miocene through Pleistocene calcareous nannofossils from low and middle latitudes. *Newsletters on Stratigraphy*, *45*(3), 221–244. https://doi.org/10.1127/0078-0421/2012/0022

Barron, J. A. (1985). Late Eocene to Holocene diatom biostratigraphy of the equatorial Pacific Ocean, Deep Sea Drilling Project Leg 85. In L. Mayer, F. Theyer, E. Thomas, et al., *Initial Reports. DSDP, 85*: Washington, DC (U. S. Govt. Printing Office), 413–456.

Barron, J. A. (1983). Latest Oligocene through early middle Miocene diatom biostratigraphy of the eastern tropical Pacific. *Marine Micropaleontology*, *7*(6), 487–515. https://doi.org/10.1016/0377-8398(83)90012-9

Beddow, H. M., Liebrand, D., Wilson, D. S., Hilgen, F. J., Sluijs, A., Wade, B. S., & Lourens, L. J. (2018). Astronomical tunings of the Oligocene–Miocene transition from Pacific Ocean Site U1334 and implications for the carbon cycle. *Climate of the Past*, *14*(3), 255–270. https://doi.org/10.5194/cp-14-255-2018

Beerling, D. J., Fox, A., & Anderson, C. W. (2009). Quantitative uncertainty analyses of ancient atmospheric CO_2 estimates from fossil leaves. *American Journal of Science*, *309*(9), 775–787. https://doi.org/10.2475/09.2009.01

Billups, K., Channell, J. E. T., & Zachos, J. (2002). Late Oligocene to early Miocene geochronology and paleoceanography from the subantarctic South Atlantic. *Paleoceanography*, *17*(1), 4-1. https://doi.org/10.1029/2000PA000568

Bradshaw, C. D., Langebroek, P. M., Lear, C. H., Lunt, D. J., Coxall, H. K., Sosdian, S. M., & de Boer, A. M. (2021). Hydrological impact of Middle Miocene Antarctic ice-free areas coupled to deep ocean temperatures. *Nature Geoscience*, *14*(6), 429–436. https://doi.org/10.1038/s41561-021-00745-w

Burke, K. D., Williams, J. W., Chandler, M. A., Haywood, A. M., Lunt, D. J., & Otto-Bliesner, B. L. (2018). Pliocene and Eocene provide best analogs for near-future climates. *Proceedings of the National Academy of Sciences of the United States of America*, *115*(52), 13288–13293. https://doi.org/10.1073/pnas.1809600115

Cramwinckel, M. J., Huber, M., Kocken, I. J., Agnini, C., Bijl, P. K., Bohaty, S. M., … Sluijs, A. (2018). Synchronous tropical and polar temperature evolution in the Eocene. *Nature*, *559*(7714), 382–386. https://doi.org/10.1038/s41586-018-0272-2

Cramwinckel, M. J., van der Ploeg, R., Bijl, P. K., Peterse, F., Bohaty, S. M., Röhl, U., … Sluijs, A. (2019). Harmful algae and export production collapse in the equatorial Atlantic during the zenith of Middle Eocene Climatic Optimum warmth. *Geology*, *47*(3), 247–250. https://doi.org/10.1130/G45614.1

Cui, Y., Schubert, B. A., & Jahren, A. H. (2020). A 23 my record of low atmospheric CO2. *Geology*, *48*(9), 888–892. https://doi.org/10.1130/G47681.1

De Vleeschouwer, D., Vahlenkamp, M., Crucifix, M., & Pälike, H. (2017). Alternating Southern and Northern Hemisphere climate response to astronomical forcing during the past 35 m. y. *Geology*, *45*(4), 375–378. https://doi.org/10.1130/G38663.1

Drury, A. J., Liebrand, D., Westerhold, T., Beddow, H. M., Hodell, D. A., Rohlfs, N., … Lourens, L. J. (2021). Climate, cryosphere and carbon cycle controls on Southeast Atlantic orbital-scale carbonate deposition since the Oligocene (30-0 Ma). *Climate of the Past*, *17*(5), 2091–2117. https://doi.org/10.5194/cp-17-2091-2021

Ellwood, B. B., Crick, R. E., El Hassani, A., Benoist, S. L., & Young, R. H. (2000). Magnetosusceptibility event and cyclostratigraphy method applied to marine rocks: Detrital input versus carbonate productivity. *Geology*, *28*(12), 1135–1138. https://doi.org/10.1130/0091-7613(2000)28<1135:MEACMA>2.0.CO;2

Fielding, C. R., Browne, G. H., Field, B., Florindo, F., Harwood, D. M., Krissek, L. A., … Pekar, S. F. (2011). Sequence stratigraphy of the ANDRILL AND-2A drillcore, Antarctica: A long-term, ice-proximal record of Early to Mid-Miocene climate, sea-level and glacial dynamism. *Palaeogeography, Palaeoclimatology, Palaeoecology*, *305*(1-4), 337–351. https://doi.org/10.1016/j.palaeo.2011.03.026

Flower, B. P., & Kennett, J. P. (1993). Relations between Monterey Formation deposition and middle Miocene global cooling: Naples Beach section. *Geology*, *21*(10), 877–880. https://doi.org/10.1130/0091-7613(1993)021<0877:RBMFDA>2.3.CO;2

Flower, B. P., & Kennett, J. P. (1994). The middle Miocene climatic transition: East Antarctic ice sheet development, deep ocean circulation and global carbon cycling. *Palaeogeography, Palaeoclimatology, Palaeoecology*, *108*(3-4), 537–555. https://doi.org/10.1016/0031-0182(94)90251-8

Foster, G. L., Lear, C. H., & Rae, J. W. B. (2012). The evolution of pCO_2, ice volume and climate during the middle Miocene. *Earth and Planetary Science Letters*, *341–344*, 243–254. https://doi.org/10.1016/j.epsl.2012.06.007

Frieling, J., Peterse, F., Lunt, D. J., Bohaty, S. M., Sinninghe Damsté, J. S., Reichart, G.-J., & Sluijs, A. (2019). Widespread Warming Before and Elevated Barium Burial During the Paleocene-Eocene Thermal Maximum: Evidence for Methane Hydrate Release? *Paleoceanography and Paleoclimatology*, *34*(4), 546–566. https://doi.org/10.1029/2018PA003425

Frieling, J., Reichart, G. J., Middelburg, J. J., Röhl, U., Westerhold, T., Bohaty, S. M., & Sluijs, A. (2018). Tropical Atlantic climate and ecosystem regime shifts during the Paleocene–Eocene Thermal Maximum. *Climate of the Past*, *14*(1), 39–55. https://doi.org/10.5194/cp-14-39-2018

Gaskell, D. E., Huber, M., O'Brien, C. L., Inglis, G. N., Acosta, R. P., Poulsen, C. J., & Hull, P. M. (2022). The latitudinal temperature gradient and its climate dependence as inferred from foraminiferal $\delta^{18}O$ over the past 95 million years. *Proceedings of the National Academy of Sciences of the United States of America*, *119*(11), 1–8. https://doi.org/10.1073/pnas.2111332119

Gilman, D. L., Fuglister, F. J., & Mitchell, J. M., Jr. (1963). On the power spectrum of "red noise". *Journal of the Atmospheric Sciences*, *20*(2), 182–184. https://doi.org/10.1175/1520-0469(1963)020<0182:OTPSON>2.0.CO;2

Gradstein, F. M., Ogg, J. G., Schmitz, M. D., & Ogg, G. M. (Eds.). (2020). *Geologic time scale 2020*. Elsevier.

Guitián, J., Phelps, S., Polissar, P. J., Ausín, B., Eglinton, T. I., & Stoll, H. M. (2019). Midlatitude Temperature Variations in the Oligocene to Early Miocene. *Paleocea-*

nography and Paleoclimatology, *34*(8), 1328–1343. https://doi.org/10.1029/2019PA003638

Herbert, T. D., Lawrence, K. T., Tzanova, A., Peterson, L. C., Caballero-Gill, R., & Kelly, C. S. (2016). Late Miocene global cooling and the rise of modern ecosystems. *Nature Geoscience*, *9*(11), 843–847. https://doi.org/10.1038/ngeo2813

Hodell, D. A., & Woodruff, F. (1994). Variations in the strontium isotopic ratio of seawater during the Miocene: Stratigraphic and geochemical implications. *Paleoceanography*, *9*(3), 405–426. https://doi.org/10.1029/94PA00292

Holbourn, A., Kuhnt, W., Clemens, S., Prell, W., & Andersen, N. (2013). Middle to late Miocene stepwise climate cooling: Evidence from a high-resolution deep water isotope curve spanning 8 million years. *Paleoceanography*, *28*(4), 688–699. https://doi.org/10.1002/2013PA002538

Holbourn, A., Kuhnt, W., Kochhann, K. G., Andersen, N., & Sebastian Meier, K. J. (2015). Global perturbation of the carbon cycle at the onset of the Miocene Climatic Optimum. *Geology*, *43*(2), 123–126. https://doi.org/10.1130/G36317.1

Holbourn, A., Kuhnt, W., Lyle, M., Schneider, L., Romero, O., & Andersen, N. (2014). Middle Miocene climate cooling linked to intensification of eastern equatorial Pacific upwelling. *Geology*, *42*(1), 19–22. https://doi.org/10.1130/G34890.1

Holbourn, A., Kuhnt, W., Schulz, M., & Erlenkeuser, H. (2005). Impacts of orbital forcing and atmospheric carbon dioxide on Miocene ice-sheet expansion. *Nature*, *438*(7067), 483–487. https://doi.org/10.1038/nature04123

Holbourn, A., Kuhnt, W., Schulz, M., Flores, J. A., & Andersen, N. (2007). Orbitally-paced climate evolution during the middle Miocene "Monterey" carbon-isotope excursion. *Earth and Planetary Science Letters*, *261*(3-4), 534–550. https://doi.org/10.1016/j.epsl.2007.07.026

Hollis, C. J., Dunkley Jones, T., Anagnostou, E., Bijl, P. K., Cramwinckel, M. J., Cui, Y., … Lunt, D. J. (2019). The DeepMIP contribution to PMIP4: Methodologies for selection, compilation and analysis of latest Paleocene and early Eocene climate proxy data, incorporating version 0.1 of the DeepMIP database. *Geoscientific Model Development*, *12*(7), 3149–3206. https://doi.org/10.5194/gmd-12-3149-2019

Hui, Z., Zhang, J., Ma, Z., Li, X., Peng, T., Li, J., & Wang, B. (2018). Global warming and rainfall: Lessons from an analysis of Mid-Miocene climate data. *Palaeogeography, Palaeoclimatology, Palaeoecology*, *512*, 106–117. https://doi.org/10.1016/j.palaeo.2018.10.025

Hüsing, S., Hilgen, F., Abdul Aziz, H., & Krijgsman, W. (2007). Completing the Neogene geological time scale between 8.5 and 12.5 Ma. *Earth and Planetary Science Letters*, *253*(3-4), 340–358. https://doi.org/10.1016/j.epsl.2006.10.036

Ji, S., Nie, J., Lechler, A., Huntington, K. W., Heitmann, E. O., & Breecker, D. O. (2018). A symmetrical CO_2 peak and asymmetrical climate change during the middle Miocene. *Earth and Planetary Science Letters*, *499*, 134–144. https://doi.org/10.1016/j.epsl.2018.07.011

Kasbohm, J., & Schoene, B. (2018). Rapid eruption of the Columbia River flood basalt and correlation with the mid-Miocene climate optimum. *Science Advances*, *4*(9), 1–8. https://doi.org/10.1126/sciadv.aat8223

Kochhann, K. G. D., Holbourn, A. E., Kuhnt, W., Channell, J. E. T., Lyle, M., Shackford, J. K., … Andersen, N. (2016). Eccentricity pacing of eastern equatorial Pacific carbonate dissolution cycles during the Miocene Climatic Optimum. *Paleoceanography*, *31*(9), 1176–1192. https://doi.org/10.1002/2016PA002988

Kodama, K. P., & Hinnov, L. A. (2014). *Rock magnetic cyclostratigraphy* (*Vol. 5*). John Wiley & Sons. https://doi.org/10.1002/9781118561294

Kürschner, W. M., Kvaček, Z., & Dilcher, D. L. (2008). The impact of Miocene atmospheric carbon dioxide fluctuations on climate and the evolution of terrestrial ecosystems. *Proceedings of the National Academy of Sciences of the United States of America*, *105*(2), 449–453. https://doi.org/10.1073/pnas.0708588105

Laskar, J., Robutel, P., Joutel, F., Gastineau, M., Correia, A. C. M., & Levrard, B. (2004). A long-term numerical solution for the insolation quantities of the Earth. *Astronomy & Astrophysics*, *428*(1), 261–285. https://doi.org/10.1051/0004-6361:20041335

Lear, C. H., Elderfield, H., & Wilson, P. (2000). Cenozoic deep-sea temperatures and global ice volumes from Mg/Ca in benthic foraminiferal calcite. *Science*, *287*(5451), 269–272. https://doi.org/10.1126/science.287.5451.269

Levy, R. H., Meyers, S. R., Naish, T. R., Golledge, N. R., McKay, R. M., Crampton, J. S., … Kulhanek, D. K. (2019). Antarctic ice-sheet sensitivity to obliquity forcing enhanced through ocean connections. *Nature Geoscience*, *12*(2), 132–137. https://doi.org/10.1038/s41561-018-0284-4

Levy, R., Harwood, D., Florindo, F., Sangiorgi, F., Tripati, R., Von Eynatten, H., … MS Science Team (2016). Antarctic ice sheet sensitivity to atmospheric CO2 variations in the early to mid-Miocene. *Proceedings of the National Academy of Sciences*, 113, 3453–3458.

Li, M., Hinnov, L., & Kump, L. (2019). Acycle: Time-series analysis software for paleoclimate research and education. *Computers & Geosciences*, *127*, 12–22. https://doi.org/10.1016/j.cageo.2019.02.011

Liebrand, D., Beddow, H. M., Lourens, L. J., Pälike, H., Raffi, I., Bohaty, S. M., … Batenburg, S. J. (2016). Cyclostratigraphy and eccentricity tuning of the early Oligocene through early Miocene (30.1–17.1 Ma): Cibicides mundulus stable oxygen and carbon isotope records from Walvis Ridge Site 1264. *Earth and Planetary Science Letters*, *450*, 392–405. https://doi.org/10.1016/j.epsl.2016.06.007

Liebrand, D., Lourens, L. J., Hodell, D. A., De Boer, B., Van de Wal, R. S. W., & Pälike, H. (2011). Antarctic ice sheet and oceanographic response to eccentricity forcing during the early Miocene. *Climate of the Past*, *7*(3), 869–880. https://doi.org/10.5194/cp-7-869-2011

Mascle, J., Lohmann, G. P., & Clift, P. D., andShipboard Scientific Party (1996). Site 959. In J. Mascle, G. P. Lohmann, P. D. Clift, et al., *Proceedings of the Ocean Drilling Program, Initial Reports, 159*: College Station, TX (Ocean Drilling Program), 65–150.

McKay, R. M., De Santis, L., Kulhanek, D. K., Ash, J. L., Beny, F., Browne, I. M., … Xiong, Z. (2019). Expedition 374 summary. *Proceedings of the International Ocean Discovery Program*.

Miller, K. G., Browning, J. V., Schmelz, W. J., Kopp, R. E., Mountain, G. S., & Wright, J. D. (2020). Cenozoic sea-level and cryospheric evolution from deep–sea geochemical and continental margin records. *Science Advances*, *6* (20), 1–15. https://doi.org/10.1126/sciadv.aaz1346

Modestou, S. E., Leutert, T. J., Fernandez, A., Lear, C. H., & Meckler, A. N. (2020). Warm middle Miocene Indian Ocean bottom water temperatures: Comparison of clumped isotope and Mg/Ca-based estimates. *Paleoceanography and Paleoclimatology*, *35*(11), 1–23. https://doi.org/10.1029/2020PA003927

Norris, R. D. (1998a). Planktonic foraminifer biostratigraphy: eastern equatorial Atlantic. In J. Mascle, G. P. Lohmann, & M. Moullade (Eds.), *Proceedings of the Ocean Drilling Program, Scientific Results, 159: College Station, TX (Ocean Drilling Program),* 445–479. https://doi.org/10.2973/odp.proc.sr.159.036.1998

Norris, R. D. (1998b). Miocene-Pliocene surface water hydrography of the eastern Equatorial Atlantic. In J. Mascle, G. P. Lohmann, & M. Moullade (Eds.), *Proceedings of the Ocean Drilling Program, Scientific Results*, *159*, 539–555. https://doi.org/10.2973/odp.proc.sr.159.021.1998

Oboh-Ikuenobe, F. E., Hoffmeister, A. P., & Chrisfield, R. A. (1999). Cyclical distribution of dispersed organic matter and dinocysts, ODP site 959 (early Oligocene-early Miocene, côte d'Ivoire-Ghana transform margin). *Palynology*, *23*(1), 87–96. https://doi.org/10.1080/01916122.1999.9989523

Pälike, H., Frazier, J., & Zachos, J. C. (2006). Extended orbitally forced palaeoclimatic records from the equatorial Atlantic Ceara Rise. *Quaternary Science Reviews*, *25* (23-24), 3138–3149. https://doi.org/10.1016/j.quascirev.2006.02.011

Pälike, H., Lyle, M. W., Nishi, H., Raffi, I., Ridgwell, A., Gamage, K., … Zeebe, R. E. (2012). A Cenozoic record of the equatorial Pacific carbonate compensation depth. *Nature*, *488*(7413), 609–614. https://doi.org/10.1038/nature11360

Pälike, H., Lyle, M., Nishi, H., Raffi, I., Gamage, K., & Klaus, A., …the Expedition 320/321 Scientists (2010). Expedition 320/321 Methods. In H. Pälike, M. Lyle, H. Nishi, I. Raffi, K. Gamage, A. Klaus, and the Expedition 320/321 Scientists, *Proceedings of the Integrated Ocean Drilling Program*, *Volume 320*/321: Tokyo (Integrated Ocean Drilling Program Management International, Inc.)

Passchier, S., Browne, G., Field, B., Fielding, C. R., Krissek, L. A., Panter, K., & Pekar, S. F. (2011). Early and middle Miocene Antarctic glacial history from the sedimentary facies distribution in the AND-2A drill hole, Ross Sea, Antarctica. *Geological Society of America Bulletin*, *123* (11-12), 2352–2365. https://doi.org/10.1130/B30334.1

Piela, C., Lyle, M., Marcantonio, F., Baldauf, J., & Olivarez Lyle, A. (2012). Biogenic sedimentation in the equatorial Pacific: Carbon cycling and paleoproduction, 12–24 Ma. *Paleoceanography*, *27*, 1–18.

Pound, M. J., Haywood, A. M., Salzmann, U., & Riding, J. B. (2012). Global vegetation dynamics and latitudinal temperature gradients during the Mid to Late Miocene (15.97–5.33 Ma). *Earth-Science Reviews*, *112*(1-2), 1–22. https://doi.org/10.1016/j.earscirev.2012.02.005

Raffi, I., Wade, B. S., Pälike, H., Beu, A. G., Cooper, R., Crundwell, M. P., … Vernyhorova, Y. V. (2020). The neogene period. In *Geologic time scale 2020* (pp. 1141–1215). Elsevier. https://doi.org/10.1016/B978-0-12-824360-2.00029-2

Raymo, M. E. (1994). The Himalayas, organic carbon burial, and climate in the Miocene. *Paleoceanography*, *9*(3), 399–404. https://doi.org/10.1029/94PA00289

Ryan, W. B. F., Carbotte, S. M., Coplan, J., O'Hara, S., Melkonian, A., Arko, R., … Zemsky, A. (2009). Global Multi-Resolution Topography (GMRT) synthesis data set. *Geochemistry, Geophysics, Geosystems*, *1*, Q03014.

Sangiorgi, F., Bijl, P. K., Passchier, S., Salzmann, U., Schouten, S., McKay, R., … Brinkhuis, H. (2018). Southern Ocean warming and Wilkes Land ice sheet retreat during the mid-Miocene. *Nature Communications*, *9*(1), 1–11. https://doi.org/10.1038/s41467-017-02609-7

Sangiorgi, F., Quaijtaal, W., Donders, T. H., Schouten, S., & Louwye, S. (2021). Middle Miocene temperature and productivity evolution at a Northeast Atlantic shelf site (IODP U1318, Porcupine Basin): Global and regional changes. *Paleoceanography and Paleoclimatology*, *36* (7), 1–19. https://doi.org/10.1029/2020PA004059

Schellpeper, M. E., & Watkins, D. K. (1998). Oligocene to early Miocene silicoflagellates from the Ivorian Basin, eastern equatorial Atlantic, Site 959. In J. Mascle, G. P. Lohmann, & M. Moullade (Eds.), *Proceedings of the Ocean Drilling Program, Scientific Results, 159*: College Station, TX (Ocean Drilling Program), 493–508.

Shafik, S., Watkins, D. K., and, & Shin, I. C. (1998). Upper Cenozoic calcareous nannofossil biostratigraphy, Côte d'Ivoire-Ghana margin, eastern equatorial Atlantic. In J. Mascle, G. P. Lohmann, & M. Moullade (Eds.), *Proceedings of the Ocean Drilling Program, Scientific Results, 159*: College Station, TX (Ocean Drilling Program), 509–523.

Shevenell, A. E., Kennett, J. P., & Lea, D. W. (2004). Middle Miocene Southern Ocean Cooling and Antarctic Cryosphere Expansion. *Science*, *305*(5691), 1766–1770. https://doi.org/10.1126/science.1100061

Shevenell, A. E., Kennett, J. P., & Lea, D. W. (2008). Middle Miocene ice sheet dynamics, deep-sea temperatures, and carbon cycling: A Southern Ocean perspective. *Geochemistry, Geophysics, Geosystems*, *9*(2), 1–14. https://doi.org/10.1029/2007GC001736

Sosdian, S. M., Babila, T. L., Greenop, R., Foster, G. L., & Lear, C. H. (2020). Ocean carbon storage across the middle Miocene: A new interpretation for the Monterey Event. *Nature Communications*, *11*(1), 1–11. https://doi.org/10.1038/s41467-019-13792-0

Sosdian, S. M., Greenop, R., Hain, M. P., Foster, G. L., Pearson, P. N., & Lear, C. H. (2018). Constraining the evolution of Neogene ocean carbonate chemistry using the boron isotope pH proxy. *Earth and Planetary Science Letters*, *498*, 362–376. https://doi.org/10.1016/j.epsl.2018.06.017

Steinthorsdottir, M., Coxall, H. K., De Boer, A. M., Huber, M., Barbolini, N., Bradshaw, C. D., … Strömberg, C. A. E. (2021a). The Miocene: The future of the past. *Paleoceanography and Paleoclimatology*, *36*(4), 1–71. https://doi.org/10.1029/2020PA004037

Steinthorsdottir, M., Jardine, P. E., & Rember, W. C. (2021b). Near-Future pCO_2 During the Hot Miocene Climatic Optimum. *Paleoceanography and Paleoclimatology*, *36*(1), 1–15. https://doi.org/10.1029/2020PA003900

Stoll, D. K., Guitian, J., Hernandez-Almeida, I., Mejia, L. M., Phelps, S., Polissar, P., … Ziveri, P. (2019). Upregulation of phytoplankton carbon concentrating mechanisms during low CO_2 glacial periods and implications for the phytoplankton pCO_2 proxy. *Quaternary Science Reviews*, *208*, 1–20. https://doi.org/10.1016/j.quascirev.2019.01.012

Super, J. R., Thomas, E., Pagani, M., Huber, M., O'Brien, C., & Hull, P. M. (2018). North Atlantic temperature and pCO_2 coupling in the early-middle Miocene. *Geology*, *46*(6), 519–522. https://doi.org/10.1130/G40228.1

Super, J. R., Thomas, E., Pagani, M., Huber, M., O'Brien, C. L., & Hull, P. M. (2020). Miocene Evolution of North Atlantic Sea Surface Temperature. *Paleoceanography and Paleoclimatology*, *35*(5), 1–15. https://doi.org/10.1029/2019PA003748

Thomson, D. J. (1982). Spectrum Estimation and Harmonic Analysis. *Proceedings of the IEEE*, *70*(9), 1055–1096. https://doi.org/10.1109/PROC.1982.12433

Tian, J., Yang, M., Lyle, M. W., Wilkens, R., & Shackford, J. K. (2013). Obliquity and long eccentricity pacing of the Middle Miocene climate transition. *Geochemistry, Geophysics, Geosystems*, *14*(6), 1740–1755. https://doi.org/10.1002/ggge.20108

Torsvik, T. H., Van der Voo, R., Preeden, U., Mac Niocaill, C., Steinberger, B., Doubrovine, P. V., … Cocks, L. R. M. (2012). Phanerozoic polar wander, palaeogeography and dynamics. *Earth-Science Reviews*, *114*(3-4), 325–368. https://doi.org/10.1016/j.earscirev.2012.06.007

Vallé, F., Westerhold, T., & Dupont, L. M. (2017). Orbital-driven environmental changes recorded at ODP Site 959 (eastern equatorial Atlantic) from the Late Miocene to the Early Pleistocene. *International Journal of Earth Sciences*, *106*(3), 1161–1174. https://doi.org/10.1007/s00531-016-1350-z

Van der Weijst, C. M., van der Laan, K. J., Peterse, F., Reichart, G.-J., Sangiorgi, F., Schouten, S., … Sluijs, A. (2022b). A 15-million-year surface-and subsurface-integrated TEX_{86} temperature record from the eastern equatorial Atlantic. *Climate of the Past*, *18*(8), 1947–1962. https://doi.org/10.5194/cp-18-1947-2022

Van der Weijst, C. M., Winkelhorst, J., de Nooijer, W., von der Heydt, A., Reichart, G.-J., Sangiorgi, F., & Sluijs, A. (2022a). Pliocene evolution of the tropical Atlantic thermocline depth. *Climate of the Past*, *18*(4), 1–13. https://doi.org/10.5194/cp-18-961-2022

Van der Weijst, C. M., Winkelhorst, J., Lourens, L., Raymo, M. E., Sangiorgi, F., & Sluijs, A. (2020). A ternary mixing model approach using benthic foraminifer $\delta^{13}C$-$\delta^{18}O$ data to reconstruct late Pliocene deep Atlantic water mass mixing. *Paleoceanography and Paleoclimatology*, •••, 35.

Van Hinsbergen, D. J., De Groot, L. V., van Schaik, S. J., Spakman, W., Bijl, P. K., Sluijs, A., … Brinkhuis, H. (2015). A paleolatitude calculator for paleoclimate studies. *PLoS One*, *10*(6), 1–21. https://doi.org/10.1371/journal.pone.0126946

Vincent, E., & Berger, W. H. (1985). Carbon dioxide and polar cooling in the Miocene: The Monterey hypothesis. In W. S. Broecker, & E. T. Sundquist (Eds.) *The carbon cycle and atmospheric CO2. Natural variations Archean to present* (*Vol. 32*, pp. 455–468). Washington: American Geophysical Union, Geophysical Monograph Series. https://doi.org/10.1029/GM032p0455

Wagner, T. (2002). Late Cretaceous to early Quaternary organic sedimentation in the eastern Equatorial Atlantic. *Palaeogeography, Palaeoclimatology, Palaeoecology*, *179*(1-2), 113–147. https://doi.org/10.1016/S0031-0182(01)00415-1

Warny, S., Askin, R. A., Hannah, M. J., Mohr, B. A., Raine, J. I., Harwood, D. M., & Florindo, F. (2009). Palynomorphs from a sediment core reveal a sudden remarkably warm Antarctica during the middle Miocene. *Geology*, *37*(10), 955–958. https://doi.org/10.1130/G30139A.1

Westerhold, T., Marwan, N., Drury, A. J., Liebrand, D., Agnini, C., Anagnostou, E., … Zachos, J. C. (2020). An astronomically dated record of Earth's climate and its predictability over the last 66 million years. *Science*, *369*(6509), 1383–1387. https://doi.org/10.1126/science.aba6853

Wilkens, R. H., Westerhold, T., Drury, A. J., Lyle, M., Gorgas, T., & Tian, J. (2017). Revisiting the Ceara Rise, equatorial Atlantic Ocean: Isotope stratigraphy of ODP Leg 154 from 0 to 5 Ma. *Climate of the Past*, *13*(7), 779–793. https://doi.org/10.5194/cp-13-779-2017

Woodruff, F., & Savin, S. (1991). Mid-Miocene isotope stratigraphy in the deep sea: High-resolution correlations, paleoclimatic cycles, and sediment preservation. *Paleoceanography*, *6*(6), 755–806. https://doi.org/10.1029/91PA02561

You, Y., Huber, M., Müller, R. D., Poulsen, C. J., & Ribbe, J. (2009). Simulation of the Middle Miocene Climate Optimum. *Geophysical Research Letters*, *36*(4), 1–5. https://doi.org/10.1029/2008GL036571

Zeebe, R. E., Westerhold, T., Littler, K., & Zachos, J. C. (2017). Orbital forcing of the Paleocene and Eocene

carbon cycle. *Paleoceanography*, *32*(5), 440–465. https://doi.org/10.1002/2016PA003054

Zeeden, C., Hilgen, F. J., Husing, S. K., & Lourens, L. J. (2014). The Miocene astronomical time scale 9–12 Ma: New constraints on tidal dissipation and their implications for paleoclimatic investigations. *Paleoceanography*, *29* (4), 296–307. https://doi.org/10.1002/2014PA002615

Zeeden, C., Hilgen, F., Röhl, U., Seelos, K., & Lourens, L. J. (2015). Sediment color as a tool in cyclostratigraphy–a new application for improved data acquisition and correction from drill cores. *Newsletters on Stratigraphy*, *48* (3), 277–285. https://doi.org/10.1127/nos/2015/0064

Zhang, Y. G., Pagani, M., Liu, Z., Bohaty, S., & DeConto, R. (2013). A 40-million-year history of atmospheric CO2. *Philosophical Transactions – Royal Society. Mathematical, Physical, and Engineering Sciences*, *371*(2001), 1–20. https://doi.org/10.1098/rsta.2013.0096

Manuscript received: July 26, 2022
Revisions required: December 12, 2022
Revised version received: January 30, 2023
Manuscript accepted: February 11, 2023

The pdf version of this paper includes an electronic supplement

Please save the electronic supplement contained in this pdf-file by clicking the blue frame above. After saving rename the file extension to .zip (for security reasons Adobe does not allow to embed .exe, .zip, .rar etc. files).

Table of contents – Electronic Supplementary Material (ESM)

Table T1: Depth conversion to rmbsf.
Table T2: List of all Early to Middle Miocene calcareous nannofossil and diatom bioevents at ODP Site 959.
Table T3: Diagnostic diatoms range chart
Table T4: Diagnostic calcareous nannofossils range chart
Table T5: Magnetic susceptibility data
Table T6: Bulk carbonate $\delta^{18}O$ and $\delta^{13}C$ data
Table T7: Wt% $CaCO_3$ data
Table T8: DeCrack mean greyscale, redness, greenness and blueness data